© Copyright 2017

Bo Zhao

Manipulating Conduction in Metal Oxide Semiconductors: Mechanism Investigation and Conductance Tuning in Doped Fe_2O_3 Hematite and Metal/Ga_2O_3/Metal Heterostructure

Bo Zhao

A dissertation

submitted in partial fulfillment of the

requirements for the degree of

Doctor of Philosophy

University of Washington

2017

Reading Committee:

Fumio S. Ohuchi, Chair

Marjorie Olmstead

Jihui Yang

Program Authorized to Offer Degree:

Materials Science & Engineering, and Nanotechnology

University of Washington

Abstract

Manipulating Conduction in Metal Oxide Semiconductors: Mechanism Investigation and Conductance Tuning in Doped Fe_2O_3 Hematite and Metal/Ga_2O_3/Metal Heterostructure

Bo Zhao

Chair of the Supervisory Committee:
Professor Fumio S. Ohuchi
Department of Materials Science & Engineering

This study aims at understanding the fundamental mechanisms of conduction in several metal oxide semiconductors, namely α-Fe_2O_3 and β-Ga_2O_3, and how it could be tuned to desired values/states to enable a wide range of applications. In the first effort, by adding Ti dopant, we successfully turned Fe_2O_3 from insulating to conductive by fabricating compositionally and structurally well-defined epitaxial α-$(Ti_xFe_{1-x})_2O_3(0001)$ films for $x \leq 0.09$. All films were grown by oxygen plasma assisted molecular beam epitaxy on $Al_2O_3(0001)$ sapphire substrate with a buffer layer of Cr_2O_3 to relax the strain from lattice mismatch. Van der Pauw resistivity and Hall effect measurements reveal carrier concentrations between 10^{19} and 10^{20} cm^{-3} at room temperature and mobilities in the range of 0.1 to 0.6 $cm^2/V\cdot s$. Such low mobility, unlike conventional band-conduction semiconductor, was attributed to hopping mechanism due to

strong electron-phonon interaction in the lattice. More interestingly, conduction mechanism transitions from small-polaron hopping at higher temperatures to variable range hopping at lower temperatures with a transition temperature between 180 to 140 K. Consequently, by adding Ti dopant, conductive Fe_2O_3 hematite thin films were achieved with a well-understood conducting mechanism that could guide further device application such as spin transistor and water splitting. In the case of Ga_2O_3, while having a band gap as high as ~5 eV, they are usually conductive for commercially available samples due to unintentional Si doping. However, we discovered the conductance could be repeatedly switched between high resistance state and low resistance state when made into metal/Ga_2O_3/metal heterostructure. However, to obtain well controlled switching process with consistent switching voltages and resistances, understanding switching mechanism is the key. In this study, we fabricated resistive switching devices utilizing a Ni/Ga_2O_3/Ir heterostructure. Bipolar switching, non-volatility, and repeatable switching are tested for the devices fabricated. Following previous discoveries on Ni/Ga_2O_3 single crystal which shows interface barrier type change (Schottky ↔ Ohmic) upon annealing accompanied by defects migration, characterization of the interface behavior on resistive switching cell Ni/Ga_2O_3(thin film)/Ir under two different resistive states was performed using X-ray photoemission spectroscopy (XPS). Most interestingly, feathers in XPS spectrum of Ga allow for a unique nondestructive approach to investigate interface by XPS through electron transparent top contact. Theoretical modeling shows that Ga migrate towards the interface upon switching to low resistive state, indicating a possible mechanism that involves interfacial switch through barrier height modifying. Such device holds potential to become the next generation of non-volatile memory device, resistive RAM.

TABLE OF CONTENTS

List of Figures iii

List of Tables vi

Chapter 1. Introduction 7

1.1 Conductivity In Metal Oxide Semiconductors 7

1.1.1 Metal oxides 7

1.1.2 Challenges in studying conductivity of metal oxides 8

1.2 Proposed Study On Alpha-Fe_2O_3 and Beta-Ga_2O_3 8

Chapter 2. Conductance Tuning In Fe_2O_3 Hematite 10

2.1 Material Background 10

2.2 Material Characterization 11

2.2.1 Composition 12

2.2.2 Crystallographic properties 12

2.2.3 Cation charge states and local structural environment 16

2.3 Electrical transport mechanism in Ti-doped Fe_2O_3 20

2.3.1 Resistivity, carrier concentration, and mobility 20

2.3.2 Comparison with transport models 22

2.3.3 The effect of growth rate on conductivity 27

2.4 Summary 29

Chapter 3. Conducance Tuning in Metal/Ga_2O_3/Metal Heterostructure - Resistive Switching ... 30

3.1 Design of Resistive Switching Cell 30

3.1.1 Introduction of resistive switching 30

3.1.2 Common switching mechanism hypotheses 31

3.1.3 Device design 31

3.2 Exploration of Switching Mechanism – Interface Probing via XPS 37

3.3 Method I: XPS Sputtering Profile 38

3.3.1 Experimental optimization 38
3.3.2 Probing of Ni/Ga_2O_3 interface via XPS sputtering profile 43
3.4 Method II: Interface Probing via XPS through Electron Transparent Top Layer 45
3.4.1 Electron escape depth 45
3.4.2 Unique case in Ga XPS 46
3.4.3 Demonstration of XPS intensity attenuation for Ga_2O_3 with Ni over layer 48
3.4.4 Probing of Ni/Ga_2O_3 Interface via XPS through Electron Transparent Layer 51
3.4.5 Proposed switching mechanism 58
3.5 Summary and Future work 60
3.5.1 Previous work summery 60
3.5.2 Continuing sputtering profile on M/Ga_2O_3/M 60
Bibliography 63

LIST OF FIGURES

Figure 2.1. (color online) PIXE spectrum for a slow-grown $(Ti_xFe_{1-x})_2O_3/Cr_2O_3/Al_2O_3$, along with a fit generated using the GUPIXWIN software package revealing x = 0.08. Inset -- final RHEED patterns for a slow-grown $(Ti_{0.08}Fe_{0.92})_2O_3$ film and a fast-grown $(Ti_{0.09}Fe_{0.91})_2O_3$ film. 12

Figure 2.2. (color online) (a) HRXRD (006) rocking curves for the fast-grown $(Ti_{0.09}Fe_{0.91})_2O_3$ film and the slow-grown $(Ti_{0.08}Fe_{0.92})_2O_3$ film. Inset: HRXRD w-2q scans of fast-grown $(Ti_xFe_{1-x})_2O_3$ films (x = 0.03, 0.05, 0.09) and a slow-grown $(Ti_{0.08}Fe_{0.92})_2O_3$ film. (b) Lattice parameters a and c for an undoped Fe_2O_3 film and the $(Ti_xFe_{1-x})_2O_3$ films. Error is estimated to be ± 0.04%. Also shown are a and c for bulk Fe_2O_3 hematite. Inset: Lattice parameters plotted against Ti concentration for slow-grown $(Ti_xFe_{1-x})_2O_3)$ films. 15

Figure 2.3. (a) Fe 2p, Ti 2p, and (b) valence band x-ray photoelectron spectra for fast-grown $(Ti_xFe_{1-x})_2O_3$ films (x = 0.03, 0.05, 0.09) and a representative slow-grown $(Ti_{0.08}Fe_{0.92})_2O_3$ film, along with spectra for a pure Fe_2O_3 film. The VB spectrum for a $(Ti_{0.15}Fe_{0.85})_2O_3$ film is shown in (b). 17

Figure 2.4. (a) Fe K-edge and (b) Ti K-edge XANES for slow-grown $(Ti_{0.08}Fe_{0.92})_2O_3$ and fast-grown $(Ti_{0.03}Fe_{0.97})_2O_3$ films, along with reference spectra for standard compounds. Inset in (b) -- overlapped Ti K-shell and Fe K-shell leading edges. (c) Fe and Ti K-edge EXAFS radial distribution functions for the same two films. 19

Figure 2.5. Resistivity vs. temperature for fast-grown $(Ti_xFe_{1-x})_2O_3$ with x = 0.03, 0.06 and 0.09. A schematic diagram of the contacts is shown in the inset. 20

Figure 2.6. (a-c) Carrier concentration vs. temperature from 190 K to 290 K for fast-grown $(Ti_xFe_{1-x})_2O_3$ with x = 0.03, 0.06 and 0.09. Inset in (a) -- V_H/I vs. magnetic field for x = 0.09 film. (d) Mobility vs. temperature determined from carrier concentration and resistivity data. 22

Figure 2.7. Fits of resistivity vs. temperature data to the small polaron hopping model from 300 K to 140 K for fast-grown $(Ti_xFe_{1-x})_2O_3$ with x = 0.03, 0.06 and 0.09. Inset -- deviation of

the experimental data from the small polaron hopping model at temperatures below 140 K is shown for x = 0.03. 24

Figure 2.8. (a) Fits of the data to the Mott 2-D variable range hopping model from 180 K to 60 K for fast-grown $(Ti_xFe_{1-x})_2O_3$ with x = 0.03, 0.06 and 0.09. (b) Fits of the resistivity data to the small polaron hopping and variable range hopping models for the $(Ti_{0.09}Fe_{0.91})_2O_3$ film, revealing a transition from one mechanism to the other, which occurs between 180 and140 K. 27

Figure 3.1. IV of Ni/Ga_2O_3 before and after annealing. 32

Figure 3.2. a) Ga_2O_3 crystal structure, b) STEM of Ga_2O_3 upon annealing, and c) cartoon of hypothesized mechanism of Ga migration. 33

Figure 3.3. Ga_2O_3 resistive switching cell. 34

Figure 3.4. Ga_2O_3 resistive switching IV characteristics. 35

Figure 3.5. Ga_2O_3 resistive switching non-volatility. 35

Figure 3.6. Ga_2O_3 resistive switching reproducibility. 36

Figure 3.7. Ni/Ti multilayer film sputtering profile. 39

Figure 3.8. Ni/Ti sputtering profile. 40

Figure 3.9. Ni sputtering edge. 41

Figure 3.10. Ti sputtering edge. 42

Figure 3.11. sputtering front and back edge of Ni. 43

Figure 3.12. Sputtering profile of virgin (solid) and switched-ON (dashed) sample of $Ni/Ga_2O_3/Ir$ resistive switching devices. 44

Figure 3.13. Sputtering profile of virgin $Ni/Ga_2O_3/Ir$ device with optimized sputtering parameters. 44

Figure 3.14. mechanism of electron escape depth. 46

Figure 3.15. Ga peaks in Ga_2O_3 XPS. 47

Figure 3.16. electron mean free path vs. kinetic energy of photoelectron. 48

Figure 3.17. Ga intensity attenuation by Ni top layer. 49

Figure 3.18. scheme of varies-thickness contact sample series. 49

Figure 3.19. Ga XPS for different Ni thickness on top. 50

Figure 3.20. XPS high resolution scan of Ga2p (a), GaLMM (b), Ga3d (c) for various thickness of top Ni contact on Ga_2O_3, and survey scan of pure Ga_2O_3 (d). 51
Figure 3.21. Ga peaks of ON(red), OFF(blue) states of 2nm Ni/Ga_2O_3, and pure Ga_2O_3 (black, signal x0.4 except for bottom right which is x 0.1). 52
Figure 3.22. ON vs OFF Ga migration. 53
Figure 3.23. peak area fitting of Ga3d. 55
Figure 3.24. peak area fitting of GaLMM... 56
Figure 3.25. peak area fitting of Ga2p. 57
Figure 3.26. resistive switching mechanism by ion migration. 58
Figure 3.27. O1s for Ga_2O_3 with different Ni thickness top layers. 61
Figure 3.28. XPS Sample Preparation Chamber.. 61

LIST OF TABLES

Table 2.1 Electrical transport summary for fast-grown $(Ti_xFe_{1-x})_2O_3$ epitaxial films. 25

Table 3.1 Calculation of Ga Migration 53

Table 3.2 work function of Ni and Ga_2O_3[82] 59

Chapter 1. INTRODUCTION

1.1 CONDUCTIVITY IN METAL OXIDE SEMICONDUCTORS

Over the past few decades, one of the most dramatic technology developments in humanity has been the application of solid state physical science to technical developments in electronic devices enabled by the invention of transistors etc. The understanding of how electricity conducts in solids led to the classification of insulator, conductor, and semiconductor. Most interestingly, within semiconductor, by understanding the mechanism of conductivity, it was made possible to tune the conductivity physically and electrically. Such understanding and discovery became the building block of the concept of computer science, in which current/charge can be controlled manually into 2 different states, known as 1 and 0. Beyond the invention of transistor, even till today, more and more attentions are drawn to this fascinating mission of manipulating charge carriers in semiconductors, giving birth to solar cell, LED, flash drive, memristor, thermoelectric device, laser, and many other crucial applications. Such quest to "*understand then alter*" the nature to our desire in order to realize many capabilities that weren't primitively presented to the world is what fundamentally motivated this research.

1.1.1 *Metal oxides*

The fast development of semiconductor technology is requiring wider range and more extreme physical and chemical properties of the material. Although elemental semiconductor like silicon and germanium are well studied and played a leading role in application into semiconductor devices, an increasing demand of new categories of materials with properties that elemental semiconductors couldn't provide is called for. Among them, compounds of metals with oxygen are one of the most promising.

Metal oxide itself is a very important class of materials that exhibits a wide range of behavior, such as bandgaps from the visible to UV, electronic properties from superconducting to metallic to semiconducting to insulating, magnetic properties from ferromagnetic to ferrimagnetic to antiferromagnetic, dielectric properties from low-k to high-k to ferroelectric to piezoelectric, and surface chemical reactivity ranging from active to inert.[1] Such diverse range of properties of metal

oxides could enable a wide range of new technologies. It has already been implemented in many fields including environmental, medical, electronic and information applications with novel devices in thermal and photocatalysis, UV-based optoelectronics, ferroelectric and resistive nonvolatile memories, spintronics, and multiferroics etc.[1] Such rich properties result from the complexities in their charge states, structures, and phase diagrams etc., and therefore can make a lot of applications that conventional semiconductors are not capable of.

1.1.2 *Challenges in studying conductivity of metal oxides*

The main goal of this research is to understand how carriers conduct in certain metal oxides, and how to tune the conductance as desired. Unlike elemental semiconductors, to study the conductivity of metal oxides exhibits many difficulties. As ionic compounds, the mechanism of transport of current carriers is rather complex. In addition to acoustic interactions, which is the characteristic of covalent bonds, one must consider optical interactions in case of oxide due to characteristic of ionic bonds.

Another difficulties lies in the preparation of the material. One of the most challenging issues in studying metal oxide is the quality of fabrication. In particular, to truly understand the nature of conductivity, one may desire a material at its purest form, namely single crystal, to rule out the complexion from grain boundaries, impurities, and other defects, making meaningful comparison of experimental results to theoretical models that are derived assuming perfect lattice case. On the other hand, upon understanding the conductivity of a material at its single crystal form, other forms of this material may be of interest due to possible desired deviation of properties from those of single crystal form, such as introduction of foreign atoms, intentional amorphous phase to allow different defects. As a result, to fabricate metal oxides into desired form has become the first and foremost problem that requires in depth study.

1.2 PROPOSED STUDY ON ALPHA-FE_2O_3 AND BETA-GA_2O_3

In the scope of this research, we aim to cover the conductivity range on both side of the spectrum, by choosing an as-is insulating oxide, Fe_2O_3, and as-is conducting oxide, Ga_2O_3 (commercially available with unintentional Si impurities). By understand the mechanism of conductivity of these

two metal oxide material systems, we can shed light on how to change the conductance to our desire to enable different applications.

Pure α-Fe_2O_3 hematite is insulating with a band gap of 2.2 eV and a corundum crystal structure. Multiple valance states of Fe can be found as 2+ or 3+ in different material systems. Pure (commercially available with Si impurities) β-Ga_2O_3 with a monoclinic structure is often conductive, despite its 5 eV band gap. When forming compound, Ga only exhibit 3+ valency.

In the attempt to make α-Fe_2O_3 conductive, the conventional way through doping is studied. In particular, we chose Ti that also exhibit multivalency in compounds (4+, 3+, 2+) as potential dopant to hopefully introduce more carriers and hence increase conductivity. However, as stated in the last section, in order to reveal the true mechanism of conduction in Ti doped Fe_2O_3, a high quality film close to single crystal form is desired. Therefore, the key challenges and questions to answer in this project are: 1) how to grow a pure α-Fe_2O_3 single crystal thin film, 2) upon introducing Ti in the growth process, how are Ti incorporated into the lattice, 3) does adding Ti change the conductivity of Fe_2O_3, and 4) what is the conducting mechanism of carriers in Ti doped Fe_2O_3.

In the attempt of making β-Ga_2O_3 insulating, it is looked from a device point of view. To utilize any semiconductor material in a device, a metal/semiconductor contact has to be formed to connect the semiconductor material to the rest of the circuit. In this study, we discovered a way of limiting the conductance by forming Ni/Ga_2O_3. Most interestingly, the magnitude of such conductance limiting effect can be tuned high or low as desired based on the voltage applied on the device. To further investigate such switching behavior, the goals we aim to achieve in this project are: 1) device fabrication of switching unit Ni/Ga_2O_3/Metal, 2) experimental characterization of possible electronical, structural changes associated with the switching, 3) derive the switching mechanism.

Chapter 2. CONDUCTANCE TUNING IN Fe_2O_3 HEMATITE

This work was performed in Environmental Molecular Sciences Laboratory, a national scientific user facility sponsored by the Office of Biological and Environmental Research of the US DOE and located at Pacific Northwest National Laboratory, collaborating with T. Kaspar, et. al. Publication of results and a detailed list of collaborators and credits can be found here[2].

2.1 MATERIAL BACKGROUND

Among the transition-metal oxides, hematite (α-Fe_2O_3) has been of significant interest due to its ubiquitous presence as an active surface for heterogeneous reactions in the terrestrial environment,[3] as well as possible utility in light-induced water splitting,[4, 5] paleomagnetic dating,[6, 7] and spin electronics.[8] Pure synthetic hematite is insulating with an experimental band-gap of ~2.2 eV.[9] With generally low conductivity limiting the usefulness of pure hematite, understanding and improving its transport properties has been of considerable interest.[10] Early experimental studies suggested that hematite exhibits an unusually low electron mobility.[10, 11] This result cannot be explained by a conventional band-like conduction picture in which itinerant electrons are delocalized and interact weakly with the lattice. Rather, a small polaron model, in which charge carriers polarize their immediate surroundings and hop between local energy minima was invoked.[12] A hopping barrier of ~0.1 eV within the *ab*-plane has emerged from several theoretical and experimental studies.[13-15] Crystallographic anisotropies in the conductivity have also been observed and attributed to spin flip scattering, which lowers the conductivity for transport along the *c* axis.[15, 16] Although progress has been made on the theoretical front, experimental studies of transport in hematite have been limited due to difficulties resulting from the generally high resistivity of hematite and ambiguities associated with measurements on polycrystalline samples.[12, 15, 17]

Natural hematite can be weakly conductive due to the presence of impurities which act as unintentional electrical dopants.[18] Thus, an effective way of improving the conductivity of hematite through intentional doping is highly desirable. Transport investigations on well-characterized epitaxial films hold many advantages over those for natural bulk hematite. Building

upon early work on the growth of pure hematite by molecular beam epitaxy (MBE) using a Cr_2O_3 buffer layer to grade the lattice mismatch and improve the crystallinity of the films,[19] Ti-doped hematite epitaxial films have been successfully deposited by oxygen-plasma-assisted molecular beam epitaxy (OPA-MBE).[8] Bench-top four-point-probe conductivity measurements with spring-loaded contacts carried out at room temperature revealed a decrease in resistivity with increasing Ti concentration. The resistivity was found to be ~25 Ω·cm at a Ti concentration of 15 cation %.[8] Other methods for synthesizing Ti-doped hematite have also been utilized, including solid-state reaction,[20] sputtering,[21] and sol-gel.[22] However, transport measurements were limited in these investigations.

In this study, our goal has been to carry out a more comprehensive investigation of the electrical conducting mechanism for well-characterized Ti-doped hematite films. To this end, we have grown and characterized Ti-doped Fe_2O_3 epitaxial films with different Ti concentrations using two different growth rates. Interestingly, despite the absence of detectable differences in structure and cation valence at the two growth rates, the electrical properties are markedly different; the films grown at the higher rate are semiconducting whereas those grown at the lower rate are highly resistive. By using a conductivity apparatus designed specifically for high-resistivity samples,[23] we have measured the temperature-dependent resistivity and Hall effect for the set of films grown at the higher rate. By making these measurements on compositionally and structurally well-defined materials, we can make meaningful comparisons with the expectations of various transport models.

2.2 Material Characterization

Surface quality was monitored during growth using reflection high-energy electron diffraction (RHEED). Charge states for Ti and Fe cations were determined by *in-situ* x-ray photoemission spectroscopy (XPS) using monochromatic Al Kα X-rays. A low-energy electron flood gun was needed for the slow-grown films due to charging on these insulating samples. Dopant concentrations were determined by proton-induced x-ray emission (PIXE) with an incident beam of 2 MeV He^+. Microstructure and lattice parameters were determined using high-resolution x-ray diffraction (HRXRD) with a Philips X'Pert diffractometer equipped with a monochromatic Cu Kα x-rays (λ = 1.54056 Å). Film thickness was measured using x-ray reflectivity (XRR). Charge states and local structure were determined by Fe and Ti K-edge x-ray absorption near-edge

spectroscopy (XANES) and extended x-ray absorption fine structure (EXAFS) on the PNC-CAT beamline at the Advanced Photon Source.

2.2.1 *Composition*

Figure 2.1 shows a PIXE spectrum for a Ti cation concentration of x = 0.08, which was determined from the areal ratio of Ti and Fe Kα peaks fitted by the GUPIXWIN package.[24] Composition determination by Rutherford backscattering spectrometry (RBS) is difficult because He ions backscattered by Cr in the Cr_2O_3 film are inelastically scattered in the overlying $(Ti_xFe_{1-x})_2O_3$ film, resulting in decreases in their kinetic energies and an overlap of the Cr and Ti peaks. To avoid this complication, all compositional information used in this paper is based on PIXE rather than RBS.

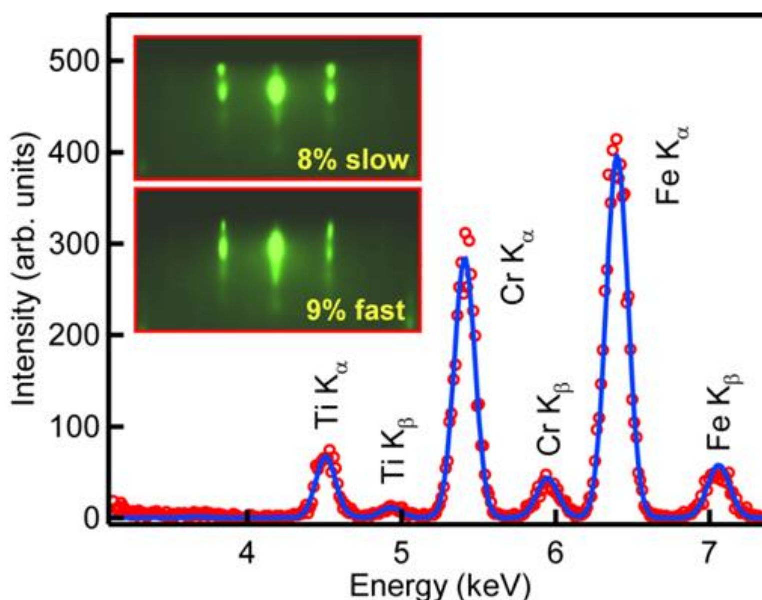

Figure 2.1. (color online) PIXE spectrum for a slow-grown $(Ti_xFe_{1-x})_2O_3/Cr_2O_3/Al_2O_3$, along with a fit generated using the GUPIXWIN software package revealing x = 0.08. Inset -- final RHEED patterns for a slow-grown $(Ti_{0.08}Fe_{0.92})_2O_3$ film and a fast-grown $(Ti_{0.09}Fe_{0.91})_2O_3$ film.

2.2.2 *Crystallographic properties*

The RHEED patterns are very similar for all films regardless of deposition rate, revealing an epitaxial orientation to the substrate. The inset of Figure 2.1 shows typical final RHEED patterns for slow- and fast-grown films with Ti concentrations of x = 0.08 and 0.09, respectively. Intensity

modulations along the streaks reveal some surface roughness, as seen in previous studies of doped and undoped hematite grown by MBE.[8, 19] This result is not unexpected considering the 1.55% in-plane lattice mismatch between bulk α-Fe_2O_3 and Cr_2O_3.

HRXRD patterns were collected from lattice planes parallel and oblique to the sample surface for both fast-grown and slow-grown Ti-doped films. These scans confirmed the single crystalline nature of the films and the epitaxial relationship with the underlying Al_2O_3 substrate. Grazing incidence XRD scans (not shown) of selected $(Ti_xFe_{1-x})_2O_3$ films revealed no secondary phases or polycrystalline reflections within the sensitivity limit of the measurement. Rocking curves of the (006) reflection for fast-grown $(Ti_{0.09}Fe_{0.92})_2O_3$ and slow-grown $(Ti_{0.08}Fe_{0.92})_2O_3$ films are shown in Figure 2.2(a). The full width at half maximum (FWHM) for each film is narrow, indicating excellent crystallinity with minimal mosaic spread. Notably, the rocking curve width is not strongly affected by the growth rate. The inset to Figure 2.2(a) shows HRXRD θ-2θ scans for fast-grown $(Ti_xFe_{1-x})_2O_3$ films (x = 0.03, 0.05, 0.09), and a slow-grown $(Ti_{0.08}Fe_{0.92})_2O_3$ film. Laue oscillations reveal a high degree of crystalline quality in all cases.[25] Two frequencies are present in these oscillations. The higher frequency oscillations are associated with the relatively thicker $(Ti_xFe_{1-x})_2O_3$ layers, which are superimposed on the lower frequency oscillations coming from the thinner Cr_2O_3 layers. The broad, low-intensity shoulder at a lower 2θ value than the sharper peak from the $(Ti_xFe_{1-x})_2O_3$ layer is associated with the Cr_2O_3 buffer layer. An ilmenite-like phase can be ruled out since $Fe_2O_3/Cr_2O_3/Al_2O_3$ deposited under the same conditions produced HRXRD patterns similar to those in the inset to Figure 2.2(a). However, it is difficult to determine the Bragg peak position for the (006) reflection of the Cr_2O_3 buffer layer due to interference from the $(Ti_xFe_{1-x})_2O_3$ film and overlapping finite thickness oscillations. An out-of-plane expansion of Cr_2O_3 would indicate residual compressive in-plane strain associated with consecutive bilayer growth of $(Ti_xFe_{1-x})_2O_3$. Interestingly, deposition of a thin Cr_2O_3 buffer layer without a hematite overlayer resulted in a completely relaxed Cr_2O_3 film (not shown) as expected; thermal expansion mismatch between the layers may play a role during sample cool-down in the $(Ti_xFe_{1-x})_2O_3/Cr_2O_3/Al_2O_3$ system.

Figure 2.2(b) plots the lattice parameters for all the $(Ti_xFe_{1-x})_2O_3$ films, determined by refining Voigt profiles simultaneously to the (1 0 10), (1 1 9), and (2 1 10) diffraction peaks. Also included are the lattice parameters for bulk hematite (a = 5.04 Å, c = 13.75 Å).[26] The lattice parameters of

the $(Ti_xFe_{1-x})_2O_3$ films were not strongly affected by growth rate. The films exhibit an expansion in the out-of-plane direction, which correlates with increasing Ti concentration. This trend is most clearly seen for the slow-grown films, as plotted in the inset to Figure 2.2(b). Ti substitution for Fe in the hematite lattice might be expected to cause lattice parameter contraction in both in-plane and out-of-plane directions, since the ionic radii for Ti^{4+} and high-spin Fe^{3+} are 0.61Å and 0.65Å, respectively.[27] However, ilmenite $FeTiO_3$, which consists of alternating layers of Ti^{4+} and Fe^{2+} in the (0001) direction, has a larger lattice (a = 5.09 Å and c = 14.08 Å)[28] than hematite. Another mechanism that can result in an out-of-plane expansion is incomplete relaxation of the epitaxial Ti-doped hematite film on the Cr_2O_3 buffer layer (a = 4.92 Å),[19] which would result in a small in-plane contraction and, therefore, an out-of-plane expansion. It is difficult to distinguish whether the observed trend with increasing Ti concentration is due to lattice expansion as the Ti-doped Fe_2O_3 film becomes more ilmenite-like, or to a change in the elastic properties of the Ti-doped Fe_2O_3 films with increasing Ti concentration which inhibits full epitaxial strain relaxation. From the lattice parameters plotted in Figure 2.2(b), it appears that a combination of these factors may be at play.

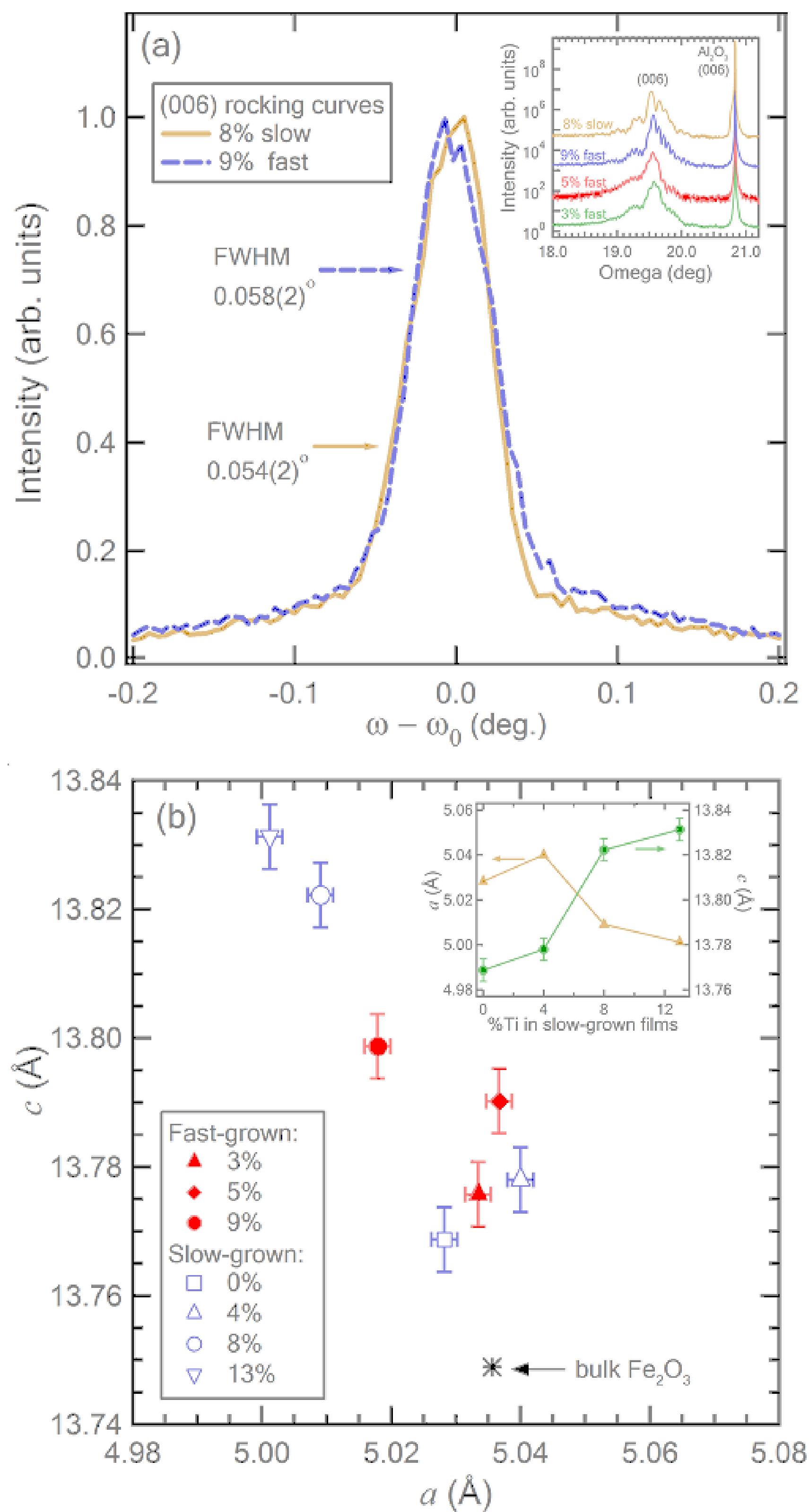

Figure 2.2. (color online) (a) HRXRD (006) rocking curves for the fast-grown $(Ti_{0.09}Fe_{0.91})_2O_3$ film and the slow-grown $(Ti_{0.08}Fe_{0.92})_2O_3$ film. Inset: HRXRD w-2q scans of

fast-grown $(Ti_xFe_{1-x})_2O_3$ films (x = 0.03, 0.05, 0.09) and a slow-grown $(Ti_{0.08}Fe_{0.92})_2O_3$ film. (b) Lattice parameters *a* and *c* for an undoped Fe_2O_3 film and the $(Ti_xFe_{1-x})_2O_3$ films. Error is estimated to be ± 0.04%. Also shown are *a* and *c* for bulk Fe_2O_3 hematite. Inset: Lattice parameters plotted against Ti concentration for slow-grown $(Ti_xFe_{1-x})_2O_3$) films.

2.2.3 *Cation charge states and local structural environment*

We show in Figure 2.3(a) high-resolution Fe 2p and Ti 2p core-level XPS spectra for three fast-grown films and a representative slow-grown $(Ti_{0.08}Fe_{0.92})_2O_3$ film. Also shown in Figure 2.3(a) is a Fe 2p reference spectrum for an undoped α-Fe_2O_3(0001) film. Spectra for the slow-grown films are identical to those for fast-grown films. Although these spectra indicate only Fe^{3+} and Ti^{4+} with no detectable Fe^{2+} or Ti^{3+}, it has been shown that the observation of states at the top of the valence band in iron oxides provides a more sensitive measure of the valence state(s) of iron.[26] Previous investigation of Ti:Fe_2O_3 thin films indicated a weak Fe^{2+} feature at the top of the valence band for x = ~0.15.[8] In the valence band spectra plotted in Figure 2.3(b), no such feature is seen up x = 0.09. However, a weak feature is observed for slow-grown $(Ti_{0.13}Fe_{0.87})_2O_3$, indicating the presence of a low concentration of Fe^{2+} in this film.

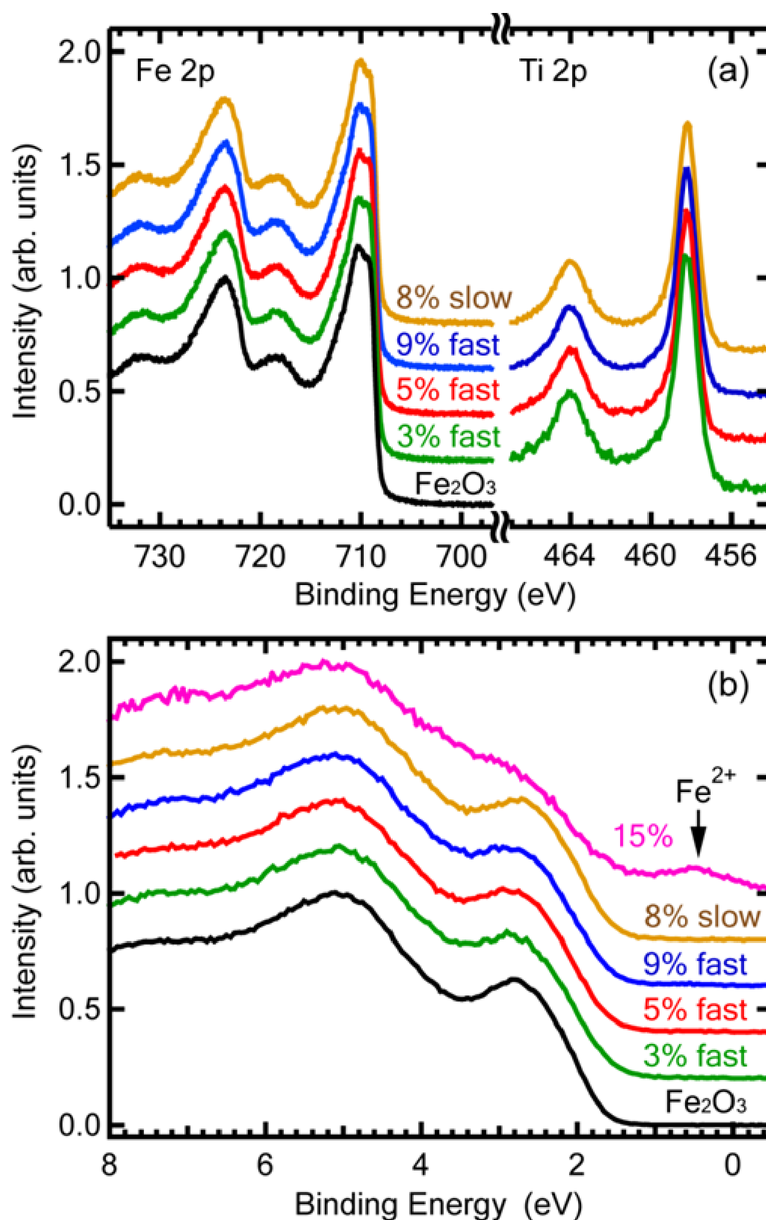

Figure 2.3. (a) Fe 2p, Ti 2p, and (b) valence band x-ray photoelectron spectra for fast-grown $(Ti_xFe_{1-x})_2O_3$ films (x = 0.03, 0.05, 0.09) and a representative slow-grown $(Ti_{0.08}Fe_{0.92})_2O_3$ film, along with spectra for a pure Fe_2O_3 film. The VB spectrum for a $(Ti_{0.15}Fe_{0.85})_2O_3$ film is shown in (b).

Similar conclusions about the cation charge states are drawn from XANES. We show in Figure 2.4(a) and (b) Fe and Ti K-edge spectra for representative slow- and fast-grown films. Comparison of the inflection point along the Fe leading absorption edge with those from reference spectra in

Figure 2.4(a) shows a strong similarity to pure α-Fe_2O_3, revealing that the vast majority of Fe is present as Fe^{3+}. Comparison of Ti K-shell XANES in Figure 2.4(b) with those for TiO_2 anatase and rutile are consistent with Ti being present as Ti^{4+}. Interestingly, the overall line shapes of the Ti K-shell XANES from the $(Ti_xFe_{1-x})_2O_3$ films more closely resemble those of the corresponding Fe K-shell XANES than those associated with the Ti K-edge for TiO_2 polymorphs, as seen in the inset of Figure 2.4(b), suggesting that Ti substitutes for Fe in the hematite lattice, rather than forming a secondary phase such as anatase or rutile. Ti substitution for Fe was further confirmed by the similarity between Ti and Fe K-edge EXAFS radial distribution functions, shown in Figure 2.4(c), which reveals that the nearest- and next-nearest-neighbor bond lengths of Ti and Fe are similar. Because of the similar values for the Ti^{4+} and Fe^{3+} ionic radii, we do not expect large changes in the local environment caused by Ti doping. Comparison of XANES and EXAFS for fast- and slow-grown films shows that they are essentially the same, indicating no substantial difference in local structure or charge states for the two growth rates, consistent with RHEED, XRD, and XPS results.

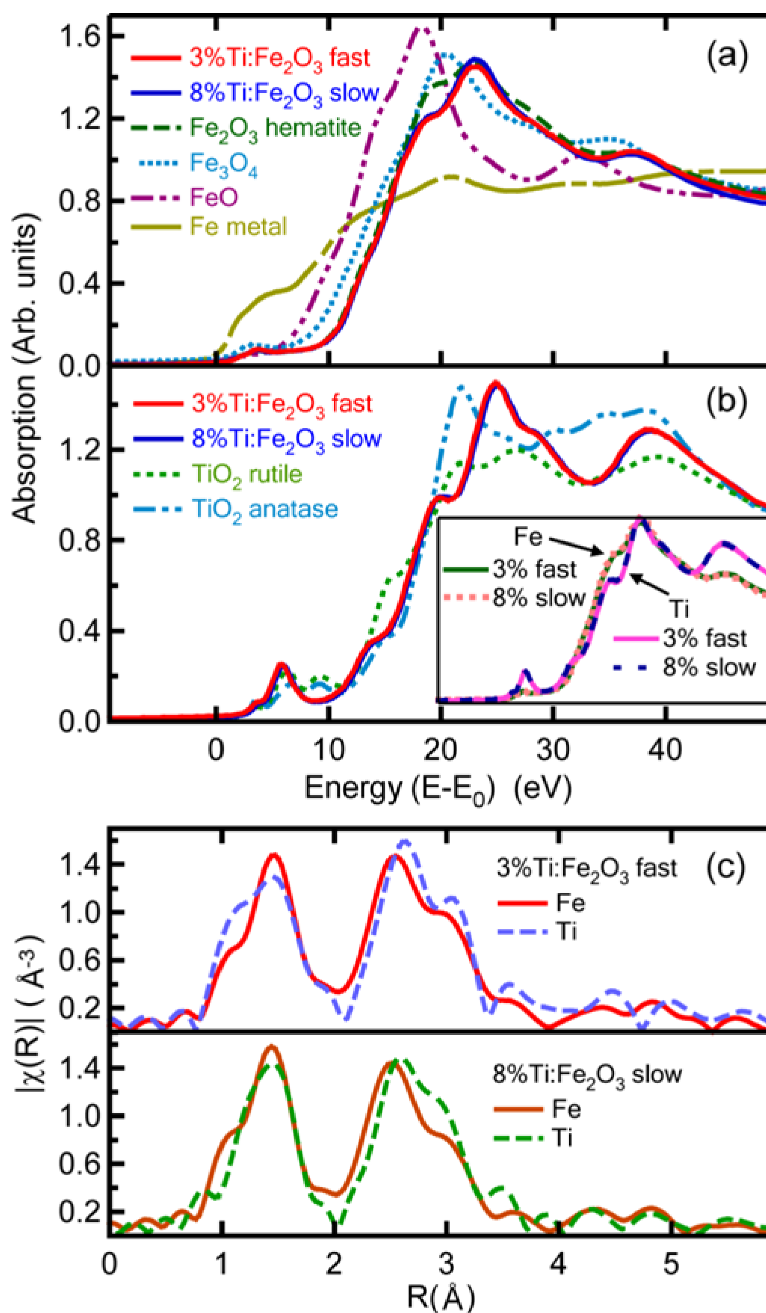

Figure 2.4. (a) Fe K-edge and (b) Ti K-edge XANES for slow-grown $(Ti_{0.08}Fe_{0.92})_2O_3$ and fast-grown $(Ti_{0.03}Fe_{0.97})_2O_3$ films, along with reference spectra for standard compounds. Inset in (b) -- overlapped Ti K-shell and Fe K-shell leading edges. (c) Fe and Ti K-edge EXAFS radial distribution functions for the same two films.

2.3 ELECTRICAL TRANSPORT MECHANISM IN TI-DOPED Fe_2O_3

2.3.1 *Resistivity, carrier concentration, and mobility*

Bench-top co-linear four-point probe measurements with spring-loaded contacts show that all Ti-doped Fe_2O_3 slow-grown films are highly resistive ($\rho \geq \sim 10^3$ Ω·cm), whereas all fast-grown Ti-doped films are modestly conductive ($\rho \sim 1$ Ω·cm) at room temperature. In contrast, pure Fe_2O_3 films grown under identical conditions at both growth rates were highly resistive. Further transport measurements were done only on the fast-grown films.

The temperature dependence of the resistivities for the fast-grown films are shown in Figure 2.5. The increases in resistivity with decreasing temperature indicate that all films are semiconducting. The room-temperature resistivities of all fast-grown $(Ti_xFe_{1-x})_2O_3$ films decrease from 1.5 to 0.3 Ω·cm with increasing x. The resistivities increase by approximately five orders of magnitude as the temperature is reduced to 50 K for all Ti concentrations.

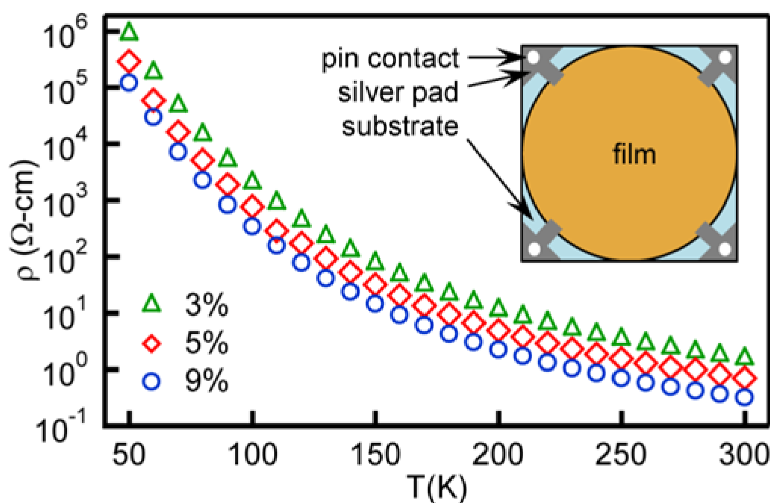

Figure 2.5. Resistivity vs. temperature for fast-grown $(Ti_xFe_{1-x})_2O_3$ with x = 0.03, 0.06 and 0.09. A schematic diagram of the contacts is shown in the inset.

The Hall data are summarized in Figure 2.6. The dependence of V_H/I on magnetic field (B) is seen in the inset of Figure 2.6(a), where the Hall coefficient is determined. The negative slope indicates

n-type conduction. The Hall coefficient (R_H) is related to the concentration and mobility of both types of carriers,[29]

$$R_H = \frac{-n\mu_e^2 + p\mu_h^2}{e(n\mu_e + p\mu_h)^2} \tag{2.1}$$

Here e is the absolute value of the electron charge, n and μ_e are the electron concentration and mobility, respectively, and p and μ_h are the hole concentration and mobility, respectively. Predominantly *n*-type conduction agrees with previous studies which reveal that electrons are the majority carrier in Ti-doped hematite.[17, 30] In addition, hole mobility in hematite has been predicted to be lower than electron mobility.[31, 32] Thus, we expect the Hall coefficient for Ti-doped hematite to be dominated by the electron terms, simplifying Eq. (2.1) to that of an intrinsic *n*-type semiconductor,

$$R_H = -\frac{1}{ne} \tag{2.2}$$

The carrier concentrations derived from the Hall coefficient using Eq. (2.2) are shown in Figure 2.6(a-c). The room-temperature carrier concentrations range from 2×10^{19} to 1×10^{20} cm^{-3}, and decrease with decreasing temperature. Hall mobilities were calculated using equation,

$$\mu = \frac{1}{e\rho n} \tag{2.3}$$

where e is the charge of an electron, ρ is resistivity, and n is carrier concentration. The results are shown in Figure 2.6(d). The mobilities for the three fast-grown films range from ~0.1 to ~0.6 $cm^2/V\cdot s$, consistent with previous experimental studies,[11, 17, 32] and do not vary significantly with temperature. Surprisingly, the carrier concentrations and mobilities do not scale with Ti concentration as one might expect based on each Ti being an uncompensated donor.

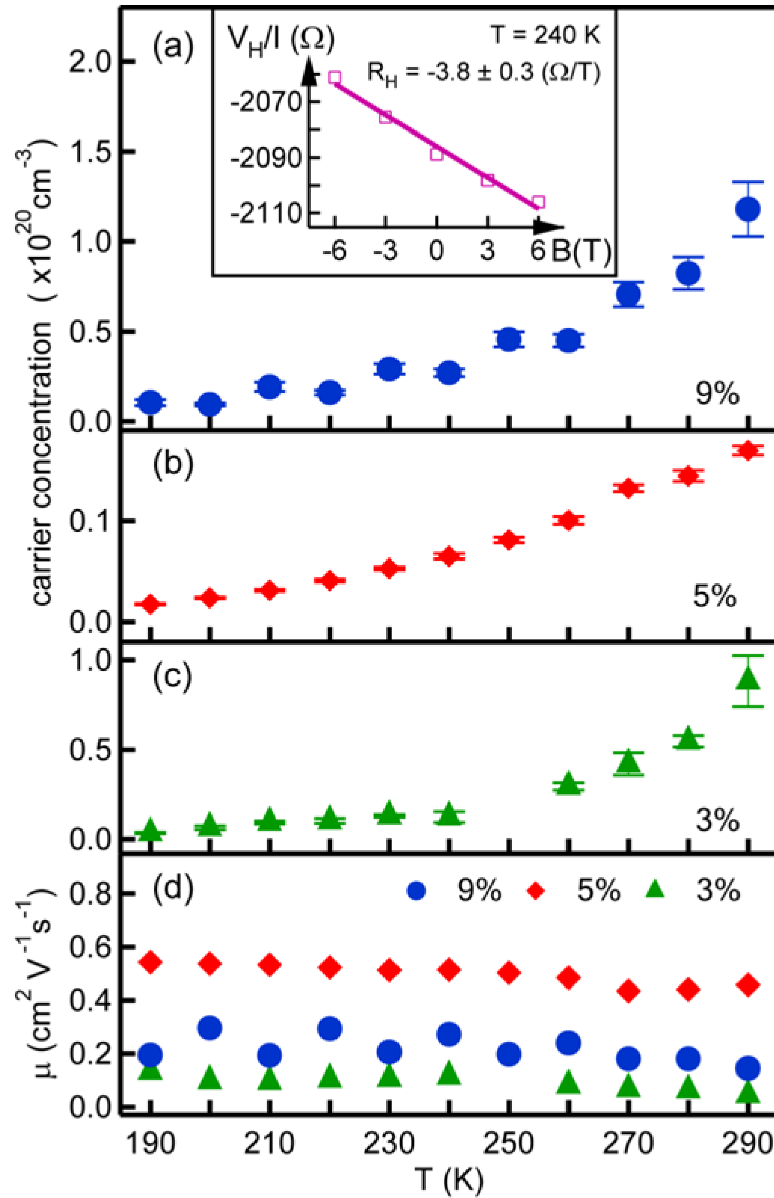

Figure 2.6. (a-c) Carrier concentration vs. temperature from 190 K to 290 K for fast-grown $(Ti_xFe_{1-x})_2O_3$ with x = 0.03, 0.06 and 0.09. Inset in (a) -- V_H/I vs. magnetic field for x = 0.09 film. (d) Mobility vs. temperature determined from carrier concentration and resistivity data.

2.3.2 *Comparison with transport models*

Different mechanisms of conduction can be explored by comparing the transport data to model predictions. In transition-metal oxides where electron-phonon coupling is usually significant due to high bond polarity, an itinerant electron tends to polarize its immediate surroundings to lower

its energies.[15] The electron and its polarized local structure constitute a quasi-particle called a polaron. The polaron effective mass is considerably higher than that of a free electron, resulting in lower electron mobility in such lattices. In most previous transport studies for hematite, the mechanism of conductivity was taken to be the small polaron hopping model at temperatures above half of the Debye temperature,[15, 33] which has been estimated to be $\Theta_D/2 \sim 200$ K.[34, 35] In this model, small polarons conduct through thermally activated hopping from one site to another. The relationship between resistivity and temperature is given by:[36]

$$\rho(T) \propto T \exp\left(\frac{E_a}{k_B T}\right) \tag{2.4}$$

Here E_a is the activation energy for hopping and k_B is the Boltzmann constant. Figure 2.7 shows small polaron model fits to the resistivity-temperature data from room temperature to 140 K for all three Ti concentrations. Activation energies determined from the slopes of the fit lines are 0.118 ± 0.002 eV, 0.116 ± 0.002 eV, and 0.116 ± 0.002 eV for x = 0.03, 0.05, and 0.09, respectively. These activation energies agree remarkably well with the 0.11 eV calculated by *ab initio* theory,[15] as well as 0.1 eV estimated for hematite basal plane conduction given by Goodenough *et al.*,[13] and 0.08 eV from Gharibi *et al.*.[14] Thus, conductivity from 300 to 140 K for all Ti concentrations is consistent with small polaron hopping and an activation barrier of ~0.1 eV. For temperatures well below $\Theta_D/2$, the small polaron hopping probability rapidly decreases and the polaron hopping model no longer applies,[37] as seen in the inset for Figure 2.7.

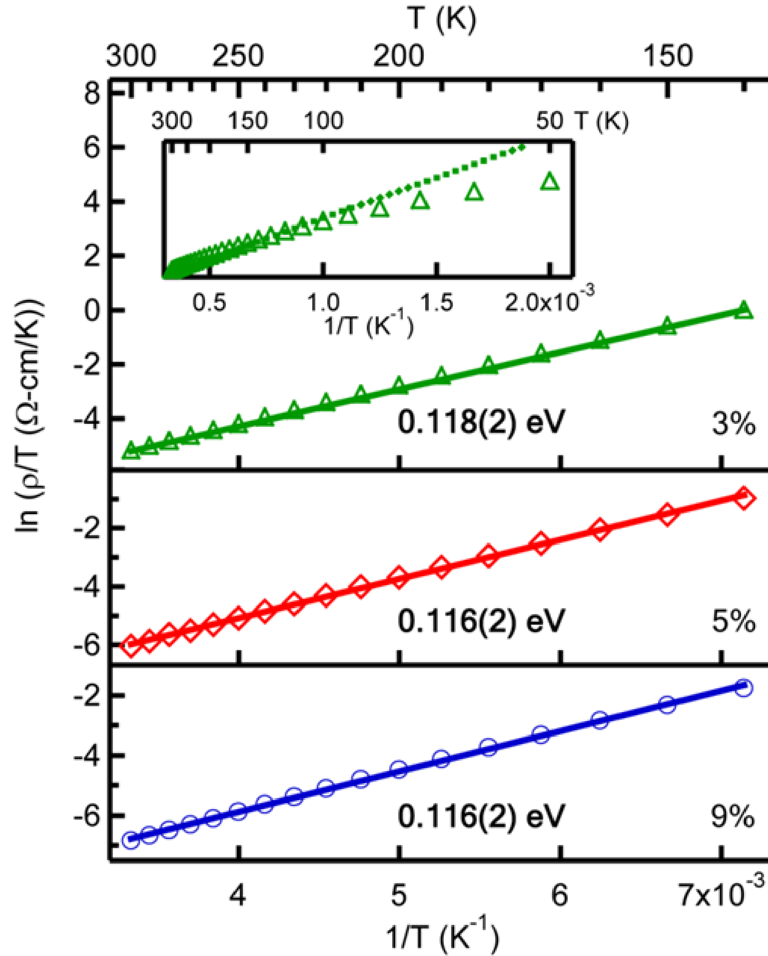

Figure 2.7. Fits of resistivity vs. temperature data to the small polaron hopping model from 300 K to 140 K for fast-grown $(Ti_xFe_{1-x})_2O_3$ with x = 0.03, 0.06 and 0.09. Inset -- deviation of the experimental data from the small polaron hopping model at temperatures below 140 K is shown for x = 0.03.

The applicability of the small polaron hopping model in the high-temperature range can also be examined using mobility data. It has been predicted that in materials where small polarons are formed, the intrinsic mobility would be of the order of 0.1 ~ 1 $cm^2/V{\cdot}s$,[38] which is lower than that of more typical semiconductors (for example, at 300 K μ_e ~7×10^3 $cm^2/V{\cdot}s$ for GaAs[39] and ~1×10^1 $cm^2/V{\cdot}s$ for La:$SrTiO_3$[40]). The mobilities for the present samples range from ~0.1 to ~0.6 $cm^2/V{\cdot}s$, comparable to that expected for small polarons. Moreover, these values are in good agreement with previous theoretical studies on hematite transport using small polaron hopping model.[15] Table

2.1 shows a summary of transport results at 290 K along with activation energies from the fits of the resistivity data to the small polaron hopping model.

Table 2.1 Electrical transport summary for fast-grown $(Ti_xFe_{1-x})_2O_3$ epitaxial films.

Film	ρ ($\Omega \cdot$cm) at 290 K	n (cm^{-3}) at 290 K	μ (V/cm$^2 \cdot$ s) at 290 K	E_a (eV) from ρ(T)
$(Ti_{0.03}Fe_{0.97})_2O_3$	1.74	8.8E + 19	0.04	0.118(2)
$(Ti_{0.05}Fe_{0.95})_2O_3$	0.80	1.7E + 19	0.46	0.116(2)
$(Ti_{0.09}Fe_{0.91})_2O_3$	0.37	1.2E + 20	0.14	0.116(2)

An alternative conduction model that is often hypothesized for doped systems is variable range hopping (VRH), in which a carrier hops between localized states created by randomly distributed dopants.[41, 42] There are several different VRH mechanisms, including Mott 3-D VRH,[41] Mott 2-D VRH,[41] and Efros-Shklovskii VRH.[43] Our data fit best with Mott 2-D VRH, for which conductivity follows the relation

$$\rho(T) \propto \exp[(T_0 / T)^{1/3}] \qquad (2.5)$$

Here $T_0 = \lambda\alpha^3 / k_B\rho_0$, where λ is a dimensionless constant, α is the coefficient of exponential decay of the localized states, ρ_0 is the density of states at the Fermi level.[42] VRH is intrinsically a low-temperature process, and the model neglects other transport mechanisms that would operate at higher temperatures, such as tunneling.[41, 42] The resistivity data can be fit well to the Mott 2-D VRH model in the low-temperature range (180 – 60 K) for all Ti concentrations. These fits are shown in Figure 2.8(a), and the quality of the fits leads us to conclude that the conduction mechanism at these relatively low temperatures is indeed VRH. Data taken at 50 K are not useful for the purpose of this fit because the films were so resistive that equilibration times were impractically long.

The fact that the data fit the Mott 2-D model better than the Mott 3-D model is not unexpected due to the magnetic structure of hematite and Hund's rules, which place spin restrictions on electron transport between adjacent Fe layers separated by an O layer along the *c* axis. In hematite, structural Fe^{3+} cations (d^5) are in a high-spin state, with all spins aligned. Moreover, all cations

within a given Fe layer in the *ab* plane have the same spin orientation, and those in adjacent Fe layers separated by an O plane along the *c* direction have the opposite spin. An electron can thus migrate from Fe to Fe along the *ab* plane without undergoing spin flip, whereas one being transported from one Fe layer to the next along the *c* direction must. In previous theoretical and experimental studies, the spin-flip energy was found to be large and the mobility along the *c* axis was approximately three orders of magnitude lower than that within the *ab* plane.[16, 31, 44] Therefore, conductivity in hematite appears to be dominated by transport within the *ab* plane, consistent with the Mott 2-D model rather than 3-D.

Finally, we show in Figure 2.8(b) the changeover in conduction mechanism across the two different temperature ranges for the $(Ti_{0.09}Fe_{0.91})_2O_3$ film. From the discussion above, we conclude that the conduction mechanism in the high-temperature regime is small polaron hopping, which transitions to Mott 2-D variable range hopping in the low-temperature regime. The transition temperature is between 180 and 140 K, comparable with the previous theoretical estimation of $\Theta_D/2$ for hematite.[34, 35] Such a transition from high-temperature SPH to low-temperature VRH has also been suggested to occur in other oxides such as Fe_3O_4,[45] Ni-doped $LaFeO_3$,[46] and Cr-doped rare-earth manganites.[47]

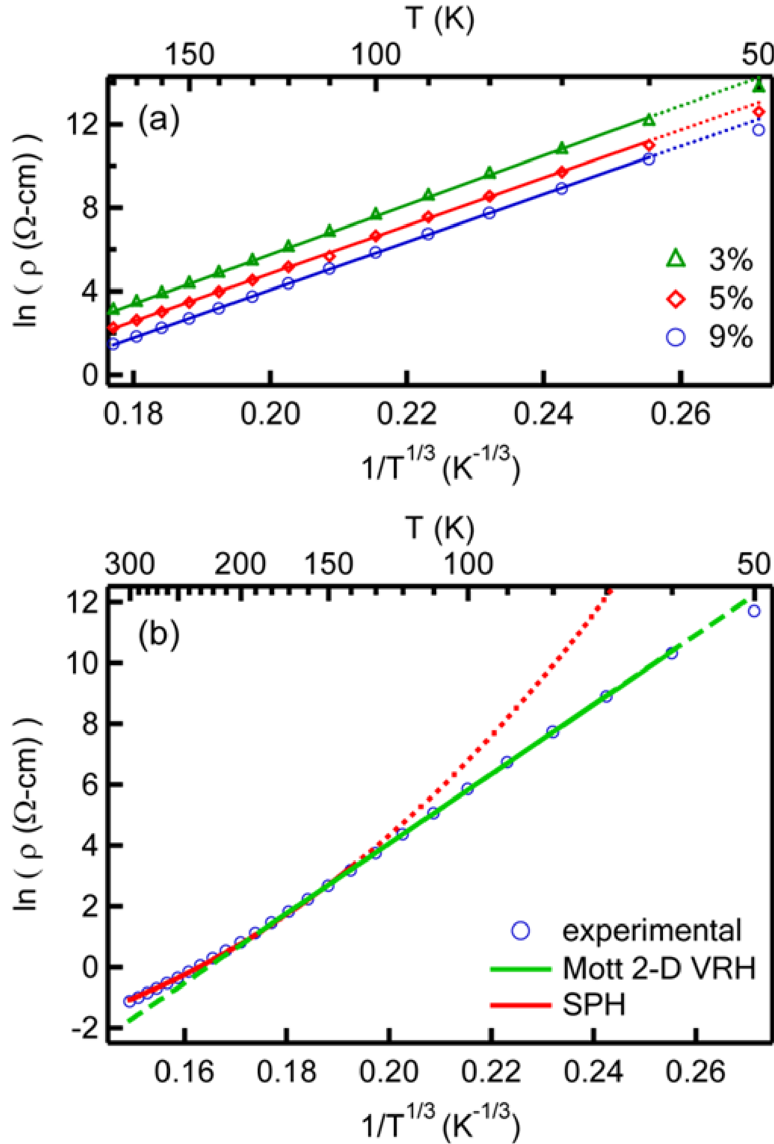

Figure 2.8. (a) Fits of the data to the Mott 2-D variable range hopping model from 180 K to 60 K for fast-grown $(Ti_xFe_{1-x})_2O_3$ with x = 0.03, 0.06 and 0.09. (b) Fits of the resistivity data to the small polaron hopping and variable range hopping models for the $(Ti_{0.09}Fe_{0.91})_2O_3$ film, revealing a transition from one mechanism to the other, which occurs between 180 and140 K.

2.3.3 *The effect of growth rate on conductivity*

The stark difference in conductivity between films grown at the two rates was unexpected. The structural and compositional properties of the two film sets are nominally the same. Yet, the fast-grown films are semiconducting whereas the slow-grown films are highly resistive at room

temperature. We conjecture that the formation of compensating cation vacancies may play a role, as has been suggested for Nb-doped TiO_2 rutile. Morris *et al.*[48] found that Nb-doped TiO_2 prepared by the solid-state reaction of NbO_2 and TiO_2 powders at elevated temperature in vacuum exhibited a Nb-derived state in the upper portion of the TiO_2 bandgap, as well as dark coloration characteristic of an *n*-type semiconductor. The same was found for diffusionally doped Nb:TiO_2(110) single crystals. In contrast, $Nb_xTi_{1-x}O_2/TiO_2(110)$ grown by OPAMBE exhibited no such gaps states, and was transparent as well as insulating.[49] A key difference between these two synthesis approaches was the oxygen fugacity at the growth front, which was suggested to significantly increase the equilibrium concentration of cation vacancies in OPAMBE grown materials, but not in materials prepared by solid-state reaction under vacuum.[48] In the present work, both growth rates employed the same oxygen pressure and plasma power settings. However, the relative oxygen overpressure and, thus, the oxygen fugacity at the growth front, is higher when the metal flux is lower (i.e. the slower growth rate). Under O-rich conditions as found in OPAMBE, the relevant charged species that could in principle form during the growth of $(Ti_xFe_{1-x})_2O_3$ are ionized substitutional Ti^{4+} dopants ($\mathrm{Ti}_{\mathrm{Fe}}^{\bullet}$), interstitial Ti^{3+} ions ($\mathrm{Ti}_{i}^{\bullet\bullet\bullet}$), structural Fe^{2+} ions ($\mathrm{Fe}_{\mathrm{Fe}}'$), interstitial Fe^{3+} ions ($\mathrm{Fe}_{i}^{\bullet\bullet\bullet}$), and Fe^{3+} vacancies ($\mathrm{V}_{\mathrm{Fe}}'''$). Using Kröger-Vink notation, charge balance requires that

$$[\mathrm{Ti}_{\mathrm{Fe}}^{\bullet}]+3[\mathrm{Fe}_{i}^{\bullet\bullet\bullet}]+3[\mathrm{Ti}_{i}^{\bullet\bullet\bullet}]+p=n+[\mathrm{Fe}_{\mathrm{Fe}}']+3[\mathrm{V}_{\mathrm{Fe}}'''] \quad (2.6)$$

Here p and n are hole and electron free carrier concentrations, respectively. Structural Fe^{2+} was shown by XPS and XANES to be negligible for all but the highest Ti concentration. Although slow-grown $(Ti_{0.13}Fe_{0.87})_2O_3$ exhibited a small concentration of Fe^{2+}, the film was highly resistive, indicating that structural Fe^{2+} does not contribute to hopping conduction. The extent of donor interstitial Fe^{3+} formation is negligible, since pure Fe_2O_3 films grown at both fast and slow growth rates are highly resistive. Interstitial Ti was determined to be negligible from characterization results presented above. However, it has been shown that cation vacancies readily form during the oxidation of magnetite (Fe_3O_4) to hematite via the intermediate maghemite (γ-Fe_2O_3), revealing that cation vacancies are stable in the various iron oxide lattices.[50] Thus, the net carrier concentration is given by

$$n - p = [\mathrm{Ti}_{\mathrm{Fe}}^{\bullet}] - 3[\mathrm{V}_{\mathrm{Fe}}'''] \quad (2.7)$$

It is clear from Eq. (2.7) that the net electron carrier concentration can range from the Ti dopant concentration to zero, depending on the extent to which cation vacancies form. First principles calculations of point defect formation energies in *n*-type ZnO reveal that the formation energy of Zn vacancies is the lowest among native point defects under oxygen-rich conditions,[51] and continues to drop with decreasing Zn/O ratio.[52] If a similar trend is followed in α-Fe_2O_3, we expect the Fe vacancy concentration to increase in films grown with lower Fe flux. Additionally, the extent of cation vacancy creation was previously concluded to be very sensitive to growth conditions such as temperature.[48] The same sensitivity in the present case could explain why the carrier concentration does not scale with Ti concentration (see Figure 2.6).

2.4 SUMMARY

We have successfully grown $(Ti_xFe_{1-x})_2O_3$ epitaxial films ($x \leq 0.13$) at two different growth rates by OPAMBE. Characterization shows good single crystallinity, charge states of Fe^{3+} and Ti^{4+} for $x \leq 0.09$, Ti substitution on Fe sites, and no substantial structural difference between films at the two growth rates. However, all fast-grown films are semiconducting whereas all slow-grown films are highly resistive. This difference is attributed to donor electron compensation by cation vacancy formation in slow-grown films, for which the oxygen-to-metal flux ratio (oxygen fugacity) is higher during growth. Resistivity and Hall measurements on fast-grown films reveal carrier concentrations of the order of $\sim 10^{19}$ -10^{20} cm^{-3} at room temperature, and mobilities of ~0.1–0.6 $V/cm^2 \cdot s$. The low mobilities and temperature dependence of the resistivity reveal a small polaron hopping conduction mechanism at higher temperature, transitioning to variable range hopping at lower temperature.

Chapter 3. CONDUCANCE TUNING IN METAL/GA_2O_3/METAL HETEROSTRUCTURE - RESISTIVE SWITCHING

3.1 DESIGN OF RESISTIVE SWITCHING CELL

3.1.1 *Introduction of resistive switching*

Resistive switching (RS) device refers to structures whose resistance can be switched reversibly by electrical stimulation. I-V characteristics of such device exhibits hysteresis. Device structure usually involves a metal-insulator-metal (MIM) sandwich structure. Typically, after preconditioning the system, it can be subsequently switched between a conductive ON state and a less conductive OFF state.[53-55] Such device has a high potential of being used as non-volatile memory, which combines functions of flash drive and DRAM (dynamic random access memory).[56-59] It is also the key feature of a new type of basic electric component called memristor, which has potential to revolutionize the architecture of future analog and digital circuit design.[60-64]

The first resistive switching prototype was made by Hickmott in 1962 based on oxide insulators. Since then, a large variety of materials in a MIM structure have been reported to show hysteresis in their I-V characteristics.[60, 65-67] The insulator in the MIM structure can be a wide range of materials including binary and multinary oxides, higher chalcogenides, and organic compounds. Depending on the different materials used in the device, the switching mechanism can be drastically different. A huge amount of effort was made throughout the past decade to figure out the mechanisms in each type of RS devices, but by far only hypothesis with partial experimental evidences are available. To fully introduce RS into mainstream semiconductor industry, thorough understanding of the switching mechanisms are needed, especially investigation of all conceivable failure mechanisms and optimization steps based on these knowledge. Thus our endeavor falls along this line that upon successful fabrication of resistive switching device prototype, investigate the switching mechanism, and compare with current hypothesis.

3.1.2 *Common switching mechanism hypotheses*

Switching mechanisms often involves a combination of physical and/or chemical processes. They can be classified roughly to different dominating effect: thermal, electronic, or ionic.[68] For thermal effect, initially the device will go through a dielectric breakdown where a conductive path is formed, equivalent to a filament, between top and bottom contacts. After the initialization, upon applying voltage, the power density locally at the filament can be extremely high, which would disrupt the filament by overheating, similar to the process of disrupting a fuse, leading to OFF state. When apply voltage again, with controlled current limit, a weak conductive filament can form again at the place where the previous rupture happened, and becoming more conductive, leading to ON state. This mechanism is also often referred to fuse-antifuse type.[69, 70] Such switch does not depend on the direction of the applied voltage and shows unipolar switching characteristic (in which on/off state can be changed under both positive voltage and negative voltage). Typical examples for such mechanism are devices made with NiO[71] and TiO_2[72]. Another popular hypothesis for switching mechanism which is supported by many experimental results is ionic effect.[7321] In such mechanism, ionic transport and electrochemical redox reactions are responsible for switching. During ON state, electrochemical reaction happens at one electrode, releasing ions that can be conducted through ion-conducting layer, forming a conductive filament path with low resistance; When the polarity of the applied voltage is reversed, the chemical equilibrium is reversed as well and ions are accumulated back into electrode, disrupting the conducting path, leading to OFF state. Typical examples for such mechanism are devices made with Ag_2S[274] and (Zn,Cd)S[75].

Nonetheless, these are just examples of a few popular hypothesis of the switching mechanisms. Whether a RS device falls into any of the category, or reveals new mechanism, are based on their experimental evidences. Our main goal in this study is to elucidate this non-traditional switching mechanism.

3.1.3 *Device design*

Designing of resistive switching unit involves choosing proper material for insulator layer and its top and bottom contacts. As discussed in the introduction section, different materials would lead

to different switching mechanism. Thickness of the insulator layer is also important in most cases. It should be thin enough to generate significant current within the voltage limit, but not so thin that a complete dielectric breakdown would happen easily.

Ga_2O_3 is a wide band gap oxide that has a unique combination of properties holding significant promise for application. While the material can function as a gate insulator, it can also be made into a transparent conductor, a photoconductor, or a chemical sensor etc. The seemingly contradicting electrical properties are results of different conducting mechanisms associated with different devices. To reveal the basic physics behind each conducting mechanism, our group has conducted a large variety of studies based on β-Ga_2O_3. Being a simple binary oxide, thermally stable before reaching melting point, and having no mixed cation valency, β-Ga_2O_3 is particularly instructive to study the link between basic physics and device potential.

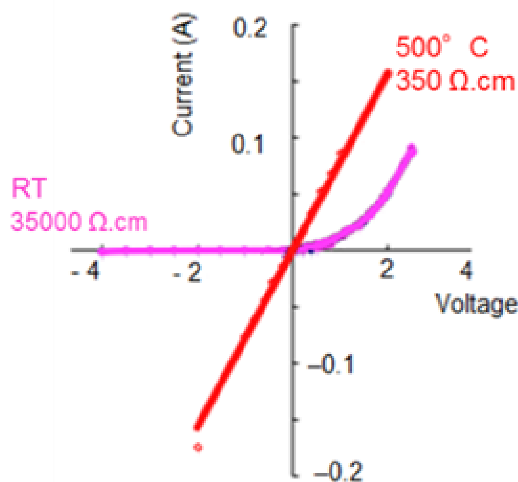

Figure 3.1. IV of Ni/Ga_2O_3 before and after annealing.

Among our past endeavors, one specific discovery shows that, upon annealing up to 500 C in vacuum of single crystal β-Ga_2O_3 with pre-deposited Ni contacts, the metal/oxide contact barrier characteristic changes from Schottky to Ohmic (Figure 3.1). Further Scanning Tunneling Microscopy (STM) reveals negatively charged quasi-particles emerged on the surface upon annealing which are most consistent with Ga vacancies (Figure 3.2b). β-Ga_2O_3 is known for its highly anisotropic crystal structure with open one-dimensional channels along b direction allowing significant ion migration (Figure 3.2a). Our proposed mechanism of such change in barrier types

is that, the original defects of Ga interstitials are thermally driven to migrate and accumulate at the interface between Ni and Ga_2O_3, creating internal field that significantly lowers the Schottky barrier, changing barrier type from Schottky to Ohmic (Figure 3.2c). A therefore interesting question arises: can we precisely control the conductivity change at room temperature by controlling such ion migration reversibly through alternating electrical field? Success will lead to a possible new type of resistive switching device with a different mechanism from that of more common filamental switching devices.

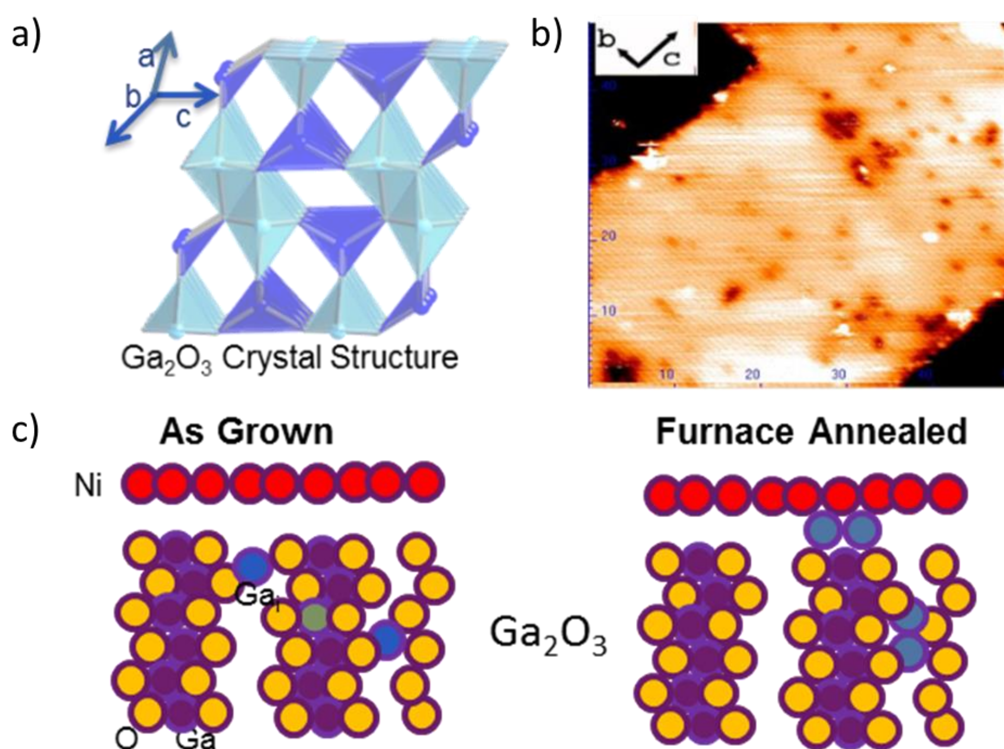

Figure 3.2. a) Ga_2O_3 crystal structure, b) STEM of Ga_2O_3 upon annealing, and c) cartoon of hypothesized mechanism of Ga migration.

Thus, our proposed device structure is Ni/Ga_2O_3/Ir, where Iridium is used as the bottom contact that has been shown to form Ohmic interface with Ga_2O_3.

<u>Device Fabrication:</u> Fabrication of the device utilizes Si wafer with 1 μm thermal oxide top insulating layer as substrate. Ir was first deposited onto the substrate via magnetron sputtering. Then Ga_2O_3 was grown via pulse laser deposition (PLD) with 248nm KrF excimer laser and

99.9999% Ga_2O_3 polycrystalline target. Substrate was at room temperature during PLD growth. X-ray diffraction (XRD) shows the Ga_2O_3 layer being amorphous. Lastly, Ni top contact was deposited on top of Ga_2O_3 layer via magnetron sputtering through a mask, creating array of 5mm diameter Ni circle contact, each of which represents a single resistive switching cell (Figure 3.3). Ellipsometry indicates the thickness of Ni, Ga_2O_3, and Ir layers to be around 50nm, 65nm, and 100nm, respectively.

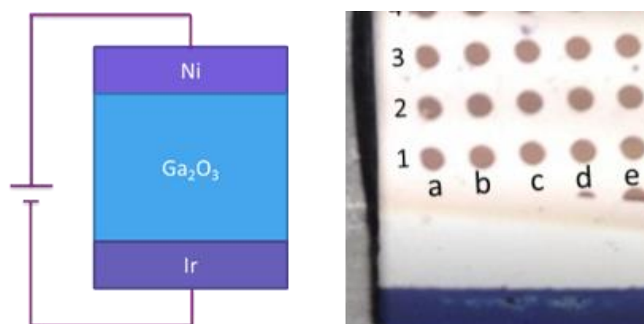

Figure 3.3. Ga_2O_3 resistive switching cell.

<u>Resistive Switching Properties:</u> Bipolar Switching: Figure 3.4 is a representative I-V characteristic of the device fabricated above. Bipolar switching behavior was observed, indicating that an ion migration, rather than thermal effect, is more likely accountable for the switching mechanism. Switching voltage is typically around -1 V and 1.5 V. One to two orders of magnitude difference in resistance between high resistive state (HRS) and low resistive state (LRS) is achieved, which is significant enough for memory device application.

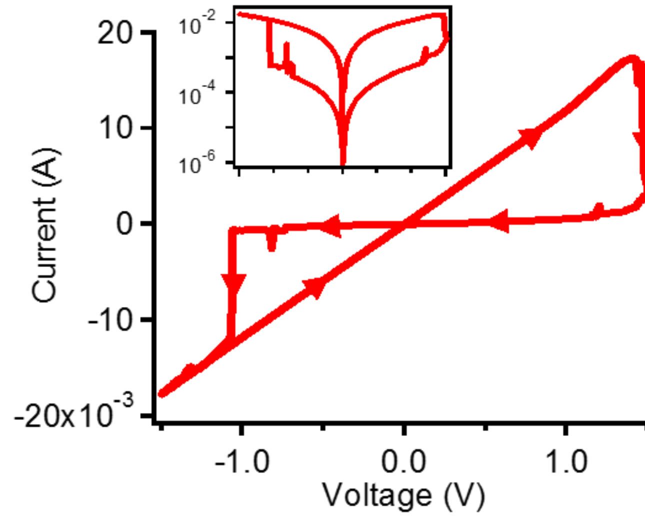

Figure 3.4. Ga_2O_3 resistive switching IV characteristics.

Non-volatility: Non-volatile property of the device was observed, i.e., after the device is being switched to either high or low resistive state, it will stay at such resistance even after removing the voltage. Probing of the resistive state with voltage sweep in the same direction as the last switching voltage confirms that the resistance stayed as the last state it was switched to, until it is switched to the other state upon applying a switching threshold voltage, as presented in Figure 3.5.

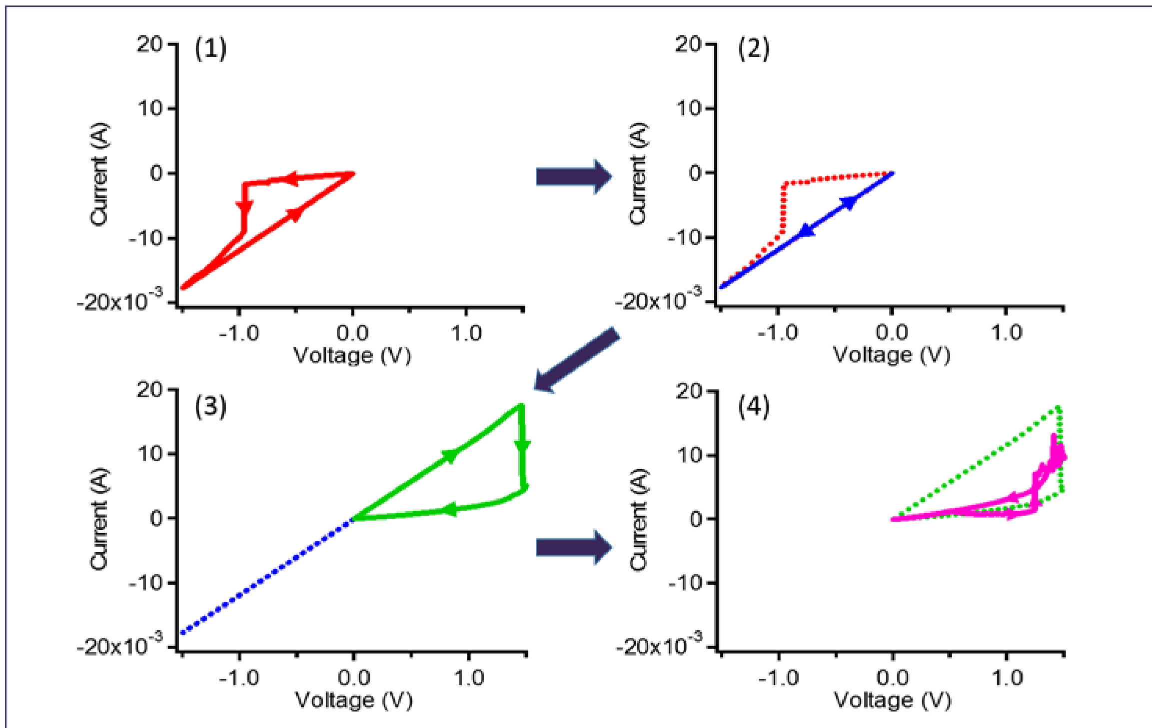

Figure 3.5. Ga_2O_3 resistive switching non-volatility.

Reproducibility: Upon several hundreds of voltage sweeps spanning several hours, the switching voltage and the resistance in HRS and LRS does fluctuate. However, no sign of degradation was shown.

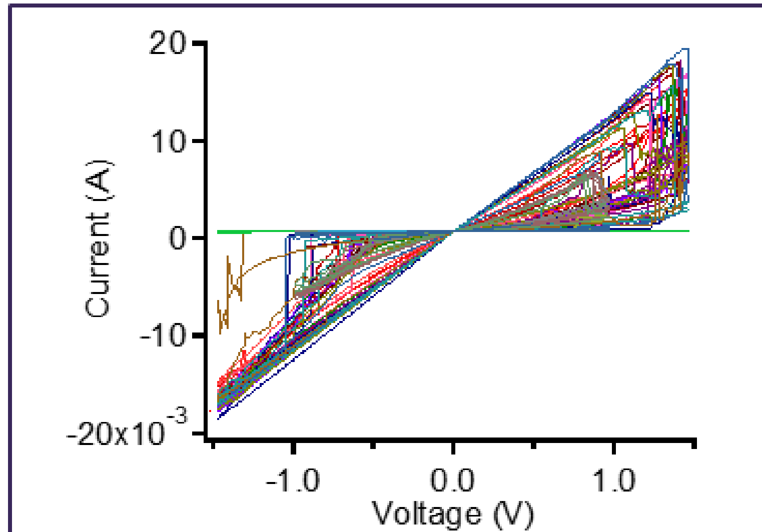

Figure 3.6. Ga_2O_3 resistive switching reproducibility.

Up to this point, we have successfully made bipolar, non-volatile resistive switching unit with good reproducibility. Careful investigation of switching mechanism are then carried on in these devices.

3.2 EXPLORATION OF SWITCHING MECHANISM – INTERFACE PROBING VIA XPS

As described in the previous section, in Ga_2O_3 system, multiple experimental and theoretical results show that a switching of conductivity was most likely due to the metal/oxide interface barrier type change upon annealing. It is hypothesized (reference Sam and Tracy) that Ga ion interstitials were driven thermally into the interface, building internal electrical field that lowers the Schottky barrier height, and eventually changing it to Ohmic contact. In resistive switching process, electrical field, instead of thermal energy, is the main driving force. Our working hypothesis of resistive switching mechanism in Ni/Ga_2O_3/Ir hetero-structure, therefore, is also through Ga ion migration in and out of the interface to modify the barrier type, driven by electrical field, switching Ni/Ga_2O_3 interface between Schottky and Ohmic reversibly.

To test the above hypothesis, an experimental technique that could probe the interface is needed, showing information of ion migration, and preferably chemical state of the ions. Very commonly, interfaces are studied via cross-section transmission electron microscopy (TEM). However, preparation of TEM sample involves cutting the sample into very thin slices so that the specimen you want to look at is of such a low density that it allows electrons to travel through. Such preparation procedure may potentially destroy the characteristic structures that differentiates resistive states, such as breaking of conducting filament path. Therefore, a probing technique that requires minimum amount of sample alteration is desired.

As a surface science technique, X-ray photoemission spectroscopy (XPS) is a powerful tool with rich information including material composition, element chemical states, and local environment etc. It would be perfect for studying resistive switching mechanism and comparing any changes in Ni, Ga, and O element between HRS and LRS. However, the limitation of XPS lies in electron escape depth. The photoelectron generated during XPS process can only travel within a few nm in the material. Therefore, only elements from the top few nm can be detected. If we want to see the Ni/Ga_2O_3 interface, we need to find some ways to work around this issue. Here we talk about two ways we used in our study.

3.3 METHOD I: XPS SPUTTERING PROFILE

In fact, people has long been using sputtering profile (also called depth profile) to compensate the shortcoming of XPS only being surface sensitive, and be able to look at layers deeper than the surface level. In principle, depth profiling uses an ion beam (Ar in our case) to etch layers of the surface to reveal subsurface information. The surface is etched by rastering an ion beam over a square or rectangular area of the sample. Before removing material from the sample, a spectrum, or set of spectra, is recorded from the surface of the sample. After the etch cycle, the ion beam is blanked and another set of spectra is recorded. This sequence of etching and spectrum acquisition is repeated until profiling has proceeded to the required depth. Combining a sequence of ion gun etch cycles with XPS analyses provides quantified information throughout the z direction (perpendicular to the film). Comparing HRS and LRS depth profiling, especially the distribution of Ga along z direction, can reveal any Ga ion migration around the interface as we hypothesized.

3.3.1 *Experimental optimization*

In practice, to obtain a high resolution depth profile that reflects true information from the film itself requires close examination of many experimental parameters involved in the sputtering process. Parameters such as ion energy, incidence angle, crater quality etc. all significantly affect how close the data is to the true nature of the film. To find the optimized parameters in depth profiling, a comprehensive study using a standard material is needed.

Here we collaborate with Zhou Yang from Mechanical Engineering at UW and propose using Ni/Ti multilayer films with well-calibrated thickness of each layer to thoroughly investigate the effect of each parameter involved in sputtering profile. Upon optimization, we will also show some interesting discoveries in Ni/Ti multilayer film depth profile to further confirm the high quality data of the optimized experimental condition.

Ideally, the sputtered region would be a well colonized hole with flat bottom surface and edges perpendicular to the surface. However, due to dispersion of the ion beam and incident angle etc., the sputtered region was more of a crater shape. Our first investigation on sputtering therefore was estimating the crater shape.

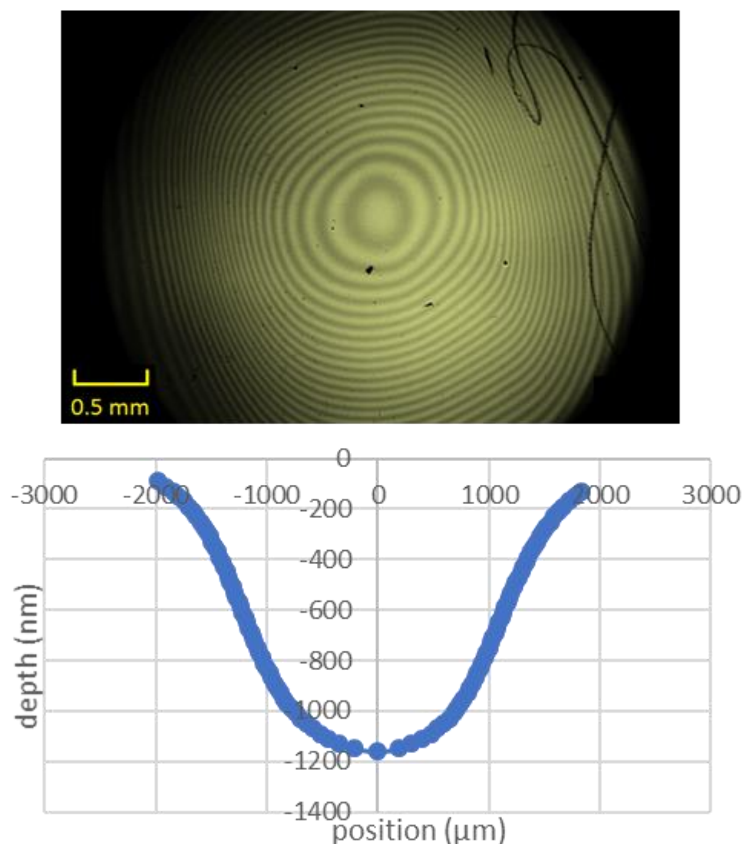

Figure 3.7. Ni/Ti multilayer film sputtering profile.

Figure 3.7(up) is an optical microscope picture of the sputtered region (no raster) using the XPS coupled with Ar sputter gun at UW mentioned above for a Ni/Ti multilayer film with 25nm thick for each layer. The darker circle represents Ni and lighter circle represents Ti due to their different reflectivity. If we record the lateral position of each layer, we would be able to generate the shape of the crater as shown in Figure 3.7(down). As we can see, the bottom surface is not completely flat, but rather curved.

One of the major errors in XPS sputtering profile is “pseudo intermixing”. Imagine if the x-ray is looking at the edge of the crater that involves film materials from different depth, it would appear averaging the XPS information across several depth layers instead of a certain depth, therefore these layers seem to “intermix”. Thus to achieve accurate depth profile, the x-ray spot need to be aligned to the center of the sputtered region where it is flat and only involves a single depth value. On this note, calibration of X-ray spot position and Ar beam center position is necessarily each time before running a sputtering profile, to make sure XPS spectra is collected at the center of the

sputtered region. Sputtering profile experiment should immediately follow the calibration process without changing the XPS chamber condition and Ar beam condition. Sample and Faraday cup (for sputtering profile calibration) can be introduced to the XPS chamber at the same time into the XPS chamber to avoid reloading and changing the chamber condition.

Besides calibration, Ar beam rastering should be used to achieve large flat sputtered area, so that X-ray spot can easily reside in the sputtered region that don't involve several depth layers. At the same time, choosing smaller x-ray spot would achieve such further, although sacrifice would have to be made for x-ray intensity and hence experiment time.

A typical sputtering profile of such film is shown in Figure 3.8**Error! Reference source not found.**. 50 nm Ni and 50nm Ti alternating layers are grown on the Si substrate. Distinct layered profile is achieved. Considering the escape depth of photoelectron is around 3 nm, the interface not being a rectangle shape is expected. When comparing the two depth profiles performed using different parameters, we can see a clear difference. Specifically, less pseudo intermixing are seen for depth profiling using smaller x-ray spot size and bigger Ar beam rastering size.

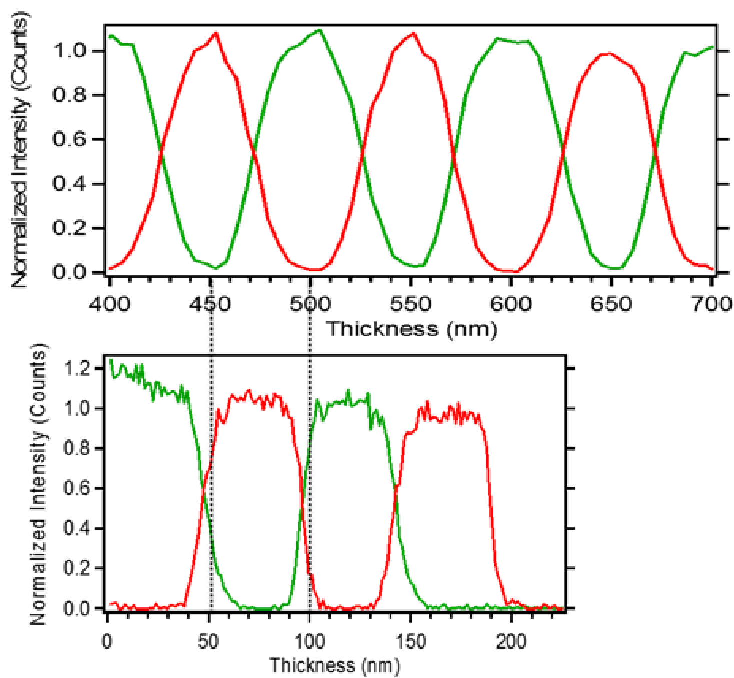

Figure 3.8. Ni/Ti sputtering profile.

Figure 3.8 is a comparison of sputtering profile induced intermixing with different sputtering parameters. The parameters are: 100um diameter x-ray spot size, 2x2 mm^2 Ar beam raster size (Figure 3.8a); and 20um diameter x-ray spot size, 5x5 mm^2 Ar beam raster size (Figure 3.8b). The two experiment are performed on well-calibrated 50nm Ni/ 50nm Ti multilayer films. We can see clearly from this figure the benefits of using smaller X-ray spot size and bigger ion beam raster size.

Another important issue is film damage by ion bombardment during the sputtering process. For minimized film damage possible, and for less chance of intermixing induced by ion beam. A smaller Ar beam power is desired.

Below is a summary of the optimized parameters that leads to the sharpest sputtering edge yet:

- 0.5 kV Ar beam power
- 20 um diameter X-ray spot
- 5x5 mm^2 rastering size

Now we look at a few more details in the Ni/Ti sputtering profile in Figure 3.8b examine the reliability of this technique.

Consistency throughout a single sputtering profile can be examined by comparing the profile of different Ni layers. (Figure 3.9, solid line is the first layer, dashed is the second layer). It is fairly consistent, showing great reliability of our sputtering process.

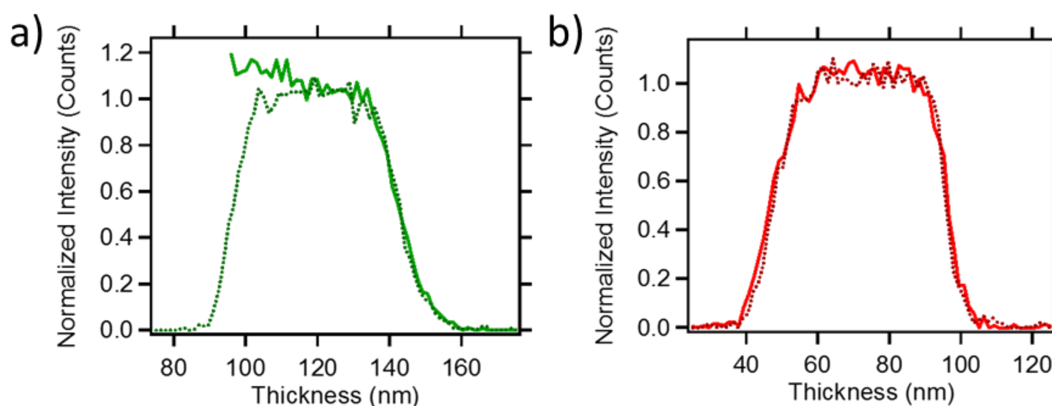

Figure 3.9. Ni sputtering edge.

Consistency can also be examined through comparing the profile of the top and bottom interface of each layer. Figure 3.10 is the comparison for the two Ti layers (dashed line is the top(closer to surface) interface, solid line is the bottom(closer to substrate) interface). We could see the consistency again in this case.

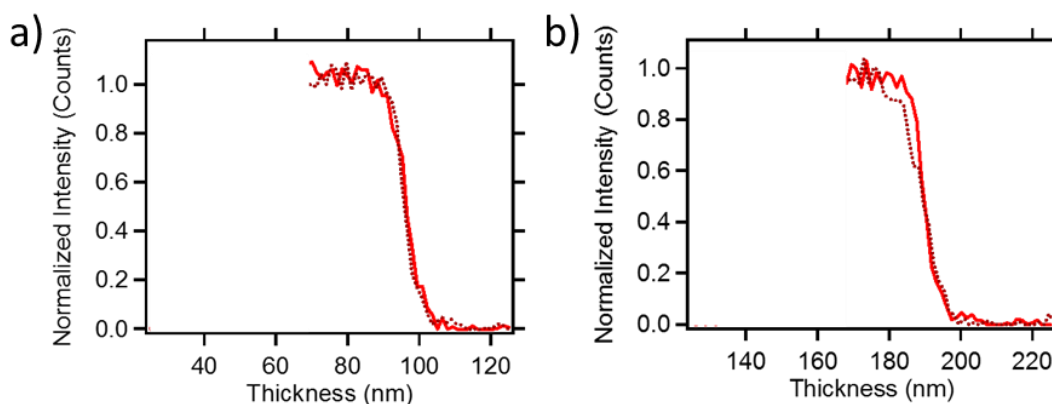

Figure 3.10. Ti sputtering edge.

However, the top and the bottom interface of the Ni layer are not exactly the same as shown in Figure 3.11 (dashed is the top interface with Ti, solid is the bottom interface sputtering profile with Ti flipped horizontally). This is because at the growth front when a Ti layer is just finished and Ni is just starting to grow, the extra enerngy that Ni still have after reaching the Ti surface will cause Ni to diffuse into the Ti layer. On the contrary, when Ni layer is finished growing and Ti starts the grow, Ti has a much smaller diffusion coeffient in Ni than Ni in Ti, and therefore will be staying on the surface without any intermixing. Therefore, the difference we see in Figure 3.11 is a perfect example of what it looks like when there is real intermixing in the sample. Such slight difference being seen in sputtering profile further proved a decent depth resolution, confirming the experimental parameters used are optimal.

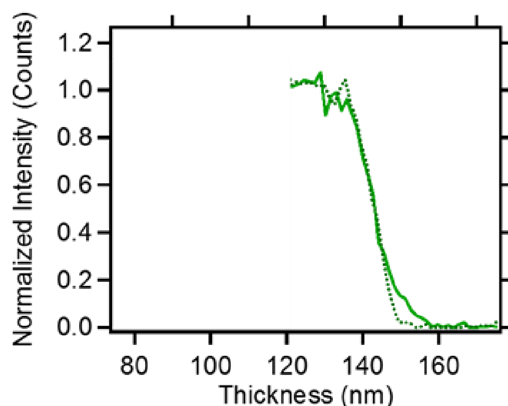

Figure 3.11. sputtering front and back edge of Ni.

3.3.2 *Probing of Ni/Ga_2O_3 interface via XPS sputtering profile*

Even before optimizing the sputtering profile technique, we had first performed sputtering profile on Ga_2O_3 resistive switching devices showing promising evidence of Ga migration across the surface after electrical treatment. While the individual data contains significant pseudo intermixing rendering the element distribution questionable, any difference shown between the two data set is, however, valid since the two sputtering profile are done under the same experimental parameters. Figure 3.12 is a comparison between as-grown sample without electrical treatment (solid line) and a switched-ON sample (dashed line). While Ni and O matched well throughout the entire probed depth region, Ga exhibits slight difference at the Ni/Ga_2O_3 interface. Ga appears to be enriched in the Ni layer after electrical treatment possibly due to Ga migration towards the surface. If so, the interface characteristic could then be modified by such migration leading to the mechanism of the switching behavior. That being said, a depth profile with much less equipment-induced intermixing is necessary to confirm such conclusion. Currently we are in the process of gaining much better quality data given the thorough investigation of depth profile optimization. Our initial result on the as-grown sample (Figure 3.13) shows promising outcome of such technique with significantly less pseudo intermixing effect.

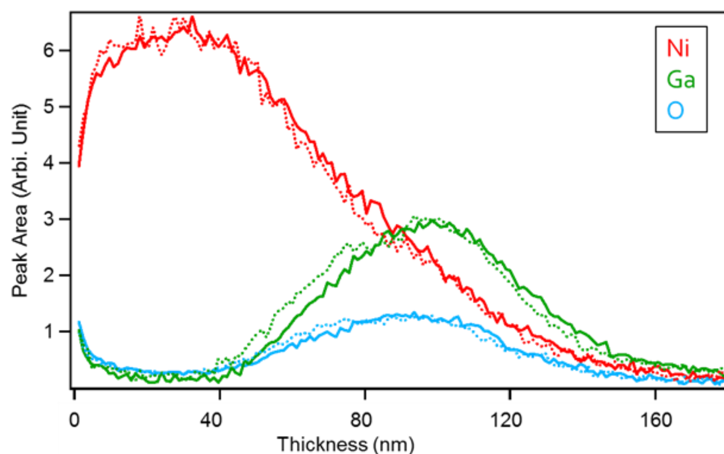

Figure 3.12. Sputtering profile of virgin (solid) and switched-ON (dashed) sample of Ni/Ga_2O_3/Ir resistive switching devices.

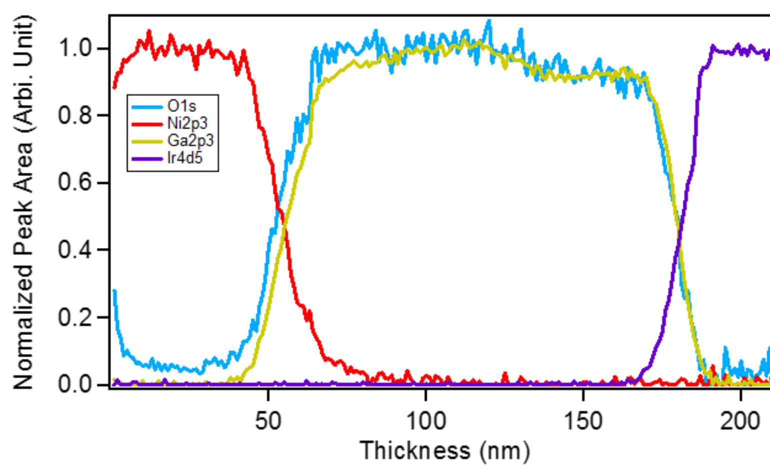

Figure 3.13. Sputtering profile of virgin Ni/Ga_2O_3/Ir device with optimized sputtering parameters.

3.4 METHOD II: INTERFACE PROBING VIA XPS THROUGH ELECTRON TRANSPARENT TOP LAYER

As we mentioned above, one of the major concerns with XPS sputtering profile is sample damaging. As low as the ion beam energy we used, there is still concern whether the sputtering process would change within the sample chemically and structurally. To reconfirm sputtering profile data, we developed a new, non-destructive method using electron escape depth to look at the interface via XPS.

3.4.1 *Electron escape depth*

After photoelectrons are generated during the XPS process, these electrons can be scattered as they are traveling in the material. There are two types of scattering that could exist. One is elastic scattering where a photoelectron keeps the same energy but changes its angle of traveling direction, which is relevant for photoelectron diffraction measurement. The other type of scattering that's happening is inelastic scattering where the kinetic energy is decreased, the process of which results in the term of electron mean free path. In inelastic scattering, the most likely case for electron to lose its energy is to generate Plasmon, which is the cause of "extrinsic" satellite that usually located at a higher binding energy than a main core level peaks in XPS. The next likely case for a photoelectron to lose its kinetic energy is to generate an electron-hole pair. The electron mean free path describes the average maximum traveling distance of an electron in a material without losing its kinetic energy. Without considering inelastic scattering, in principle, the higher the kinetic energy the electron has, the higher the mean free path is. However, Plasmon and electron-hole pair generation process can absorb the electrons who have enough kinetic energies (above a few tens of eV). As a result, these two factors compete with each other, determining the electron mean free path together. A relationship between electron mean free path and its kinetic energy are plotted in Figure 3.14 (left). We can see from the plot that below 50 eV, the inelastic scattering process are dominating as the kinetic energy electrons getting big enough to excite Plasmon or electron-hole pair, hence having less and less mean free path. As the kinetic energy of electron goes higher, the inelastic scattering process are dominating and the mean free path increases with increasing kinetic energy.

As a result of elastic and inelastic scattering, as shown in Figure 3.14(right), not all of the photoelectrons generated at a depth d below the surface can make it to the analyzer. If we define the escape depth (some also call it electron attenuation length (EAL)), λ, is that depth at which the probability of escape is reduced to 1/e (~36.8%) compared to emission from an atom at the surface (d=0), we will have:

$$\boldsymbol{I(d) = I(0)\, e^{-\frac{d}{\lambda \sin\theta}}} \tag{3.1}$$

Where I(0) is the original XPS intensity generated, I(d) is the XPS intensity after being attenuated by a thickness of d and a take off angle of θ with respect to the surface plane.

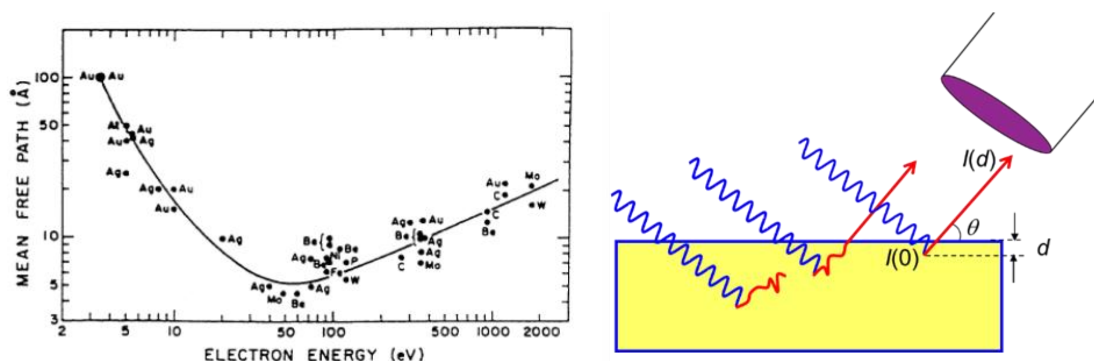

Figure 3.14. mechanism of electron escape depth.

The theoretical derivation of escape depth is not trivial. It involves a lot of factors such as materials, photoionization asymmetry parameter, etc..[76] It can be calculated from analytical expressions derived from solution of the kinetic Boltzmann equation within the transport approximation.[76-80] In practice, one may look up a specific value from literature. NIST Electron Effective-Attenuation-Length Database is a rather reliable source which is a software takes into account many input parameters such as materials, analyzer angle, incident x-ray angle, etc., and generates a calculated value from its own data base. The escape depth values are all obtained from this sourse.[81]

3.4.2 *Unique case in Ga XPS*

Escape depth can be critically useful in certain cases which can give a lot of interesting information from XPS about the material. Shown in ***Error! Reference source not found.*** is a typical survey scan of Ga_2O_3.

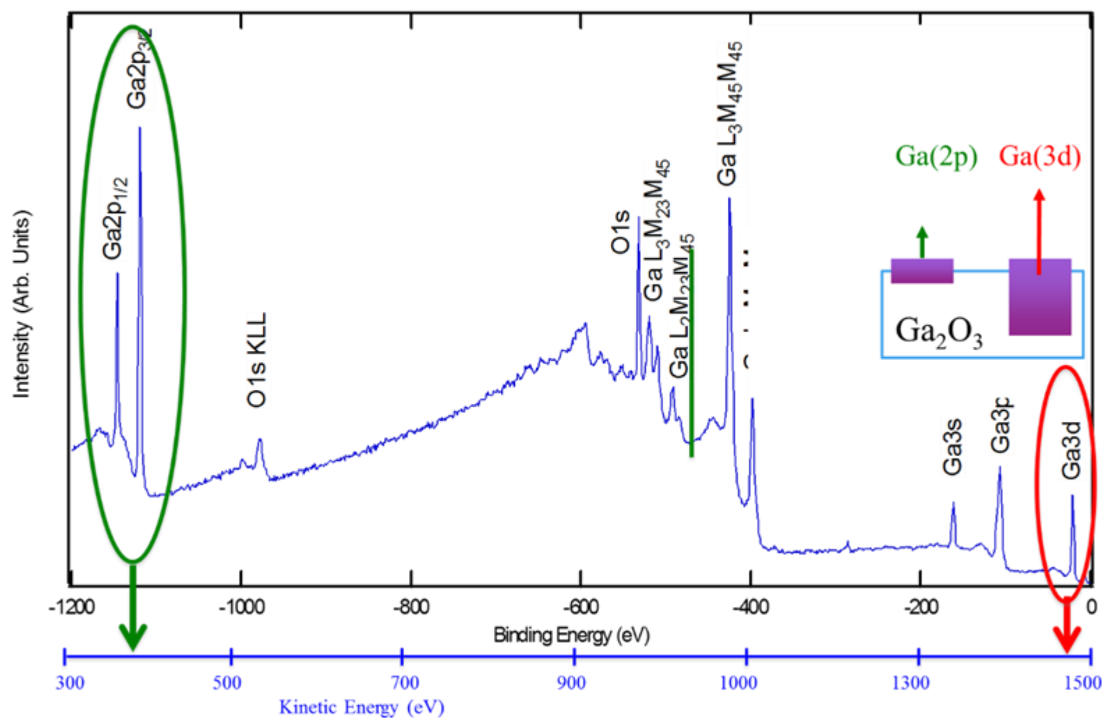

Figure 3.15. Ga peaks in Ga_2O_3 XPS.

Two prominent peaks, Ga2p and Ga3d, are of most practical use for Ga XPS analysis because of their simple shapes and high intensities. What's vastly interesting about these two peaks are that they are tremendously far apart from each other in binding energies. Ga3d in Ga_2O_3 has a very low binding energy, usually around 21 eV. For incident x-ray energy of 1486.6 eV, and assuming the work function of Ga_2O_3 is around 4 eV, the kinetic energy of such photoelectrons is about 1486.6 – 21 – 4 = 1461.6 eV. Whereas for Ga 2p who has a very high binding energy of 1118.5 eV, the corresponding kinetic energy is about 368 eV. Such huge difference in kinetic energies would potentially lead to very different escape depths. Indeed, by looking up values from NIST[81], for Ni over layers, Ga 3d has an escape depth of ~ 1.645 nm, and Ga 2p has an escape depth of ~ 0.550 nm. Such huge difference in escape depths for different prominent peaks in the same element is not often seen, which enables a wide range of unique analysis. Which will be shown in the following two sections.

3.4.3 *Demonstration of XPS intensity attenuation for Ga_2O_3 with Ni over layer*

Photoelectron created during the XPS process has an escape depth on the order of nm. This means XPS spectrum is looking at everything from the top surface to this depth. This gives us the opportunity to probe the contact layer, semiconductor layer, and their interface all at once if the thickness of the top contact layer is comparable to the escape depth. More interestingly, since photoelectron with different kinetic energy has different escape depth as shown in Figure 3.15. By looking at the photoemission from the same element at different binding energies, the escape depth would be different. This could lead to very useful information, such as reverse-construction of the element distribution at different depth. Particularly, Ga has two peaks that are far apart from each other. Such distinctive separation allows us to identify whether the Ga we see is at the surface or interface. Quantitative model can also be developed to extract how deep the Ga is below the surface (for take off angle at 45 degree), as shown in Figure 3.17. Furthermore, if there is Ga migration towards or away from interface, there will be a difference in the change of intensity for different Ga peaks. Utilizing such technique, we will be able to detect the change at interface between HRS and LRS without destroying the sample.

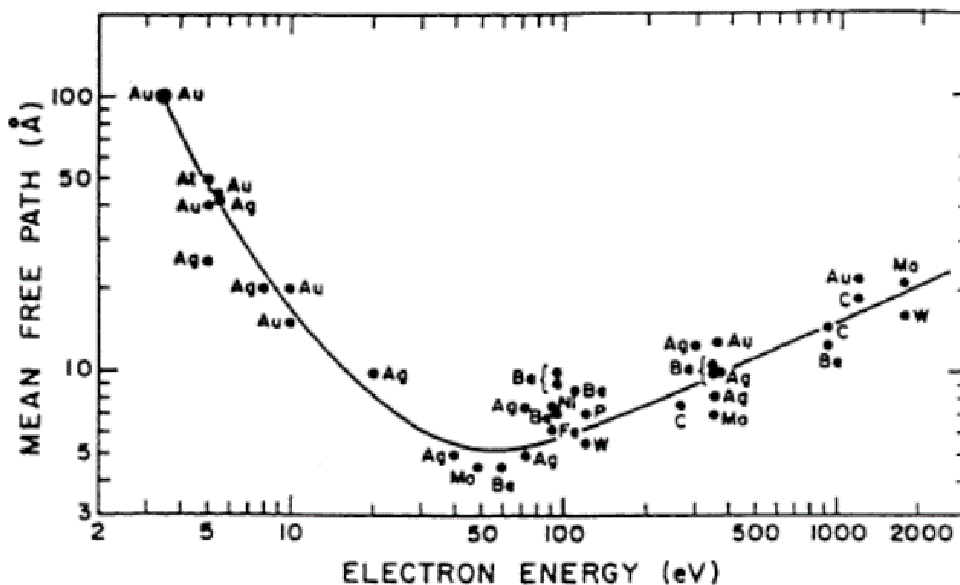

Figure 3.16. electron mean free path vs. kinetic energy of photoelectron.

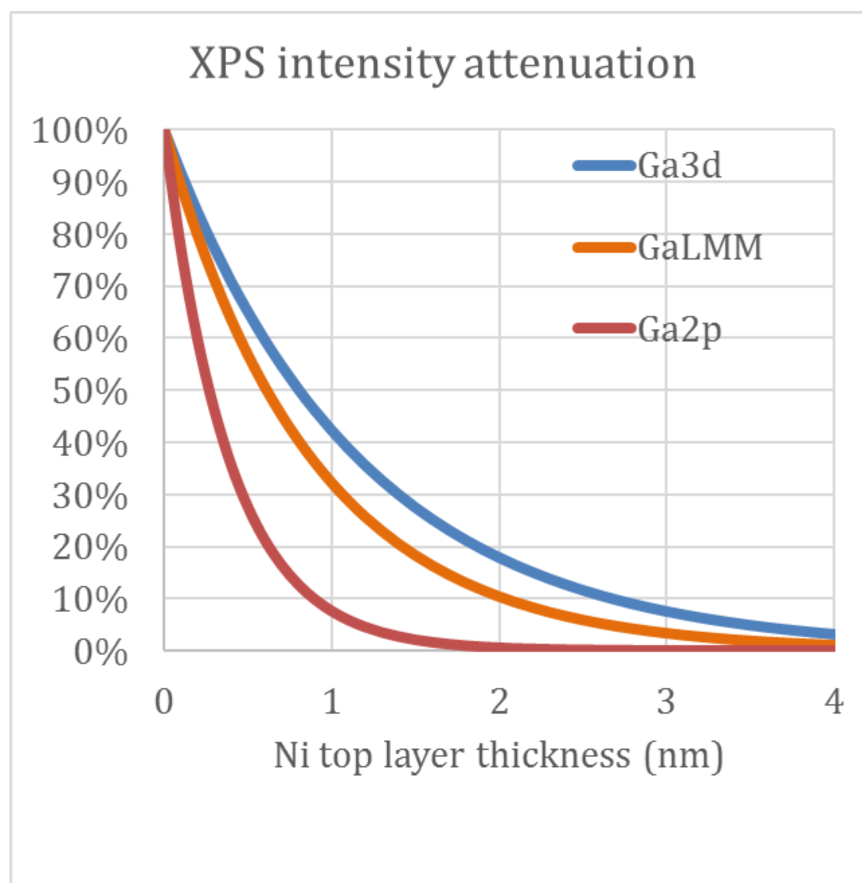

Figure 3.17. Ga intensity attenuation by Ni top layer.

To demonstrate the attenuation effect, Figure 3.18 is an illustration of such series of devices grown (not drawn to scale). As shown in the figure, 5 different thickness of Ni contact is sputtered on top of Ga_2O_3 and put in sample box then transferred into the XPS together. The total exposure time to air is around 20 min.

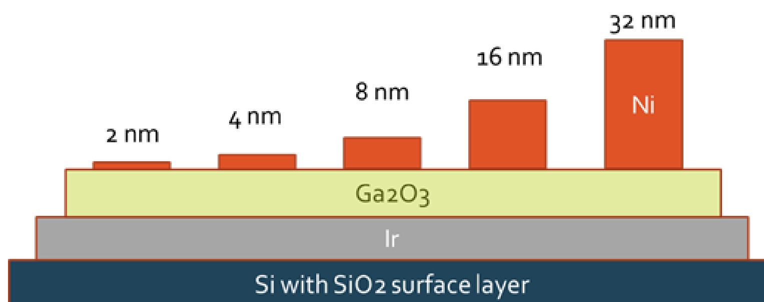

Figure 3.18. scheme of varies-thickness contact sample series.

Figure 3.18 shows the high resolution XPS of Ga for the as grown sample from above, together with a survey spectra of pure Ga_2O_3 showing the binding energies of each Ga peak. Comparison

of the Ga3d peak for 5 samples reveals that Ga peak can be seen for the 2nm Ni sample, and only trace amount can be seen for the 4nm Ni contact sample. Above 4 nm of Ni, no Ga3d can be seen. This is consistent with the electron escape depth of ~2nm at binding energy of 21 eV. Furthermore, we see similar results for GaLMM spectra with main Auger peak at 425 eV with an escape depth of 1.5 nm. What's even more interesting is Ga2p spectra at binding energy of 1120eV. Since the escape depth at this binding energy is as low as 1nm, even the thinnest Ni contact sample shows no intensity of Ga2p peak. This gives us confidence that the growth of the thin Ni contact was uniformly covering the device region with no agglomeration, unlike a lot of other cases in metal layer growth.

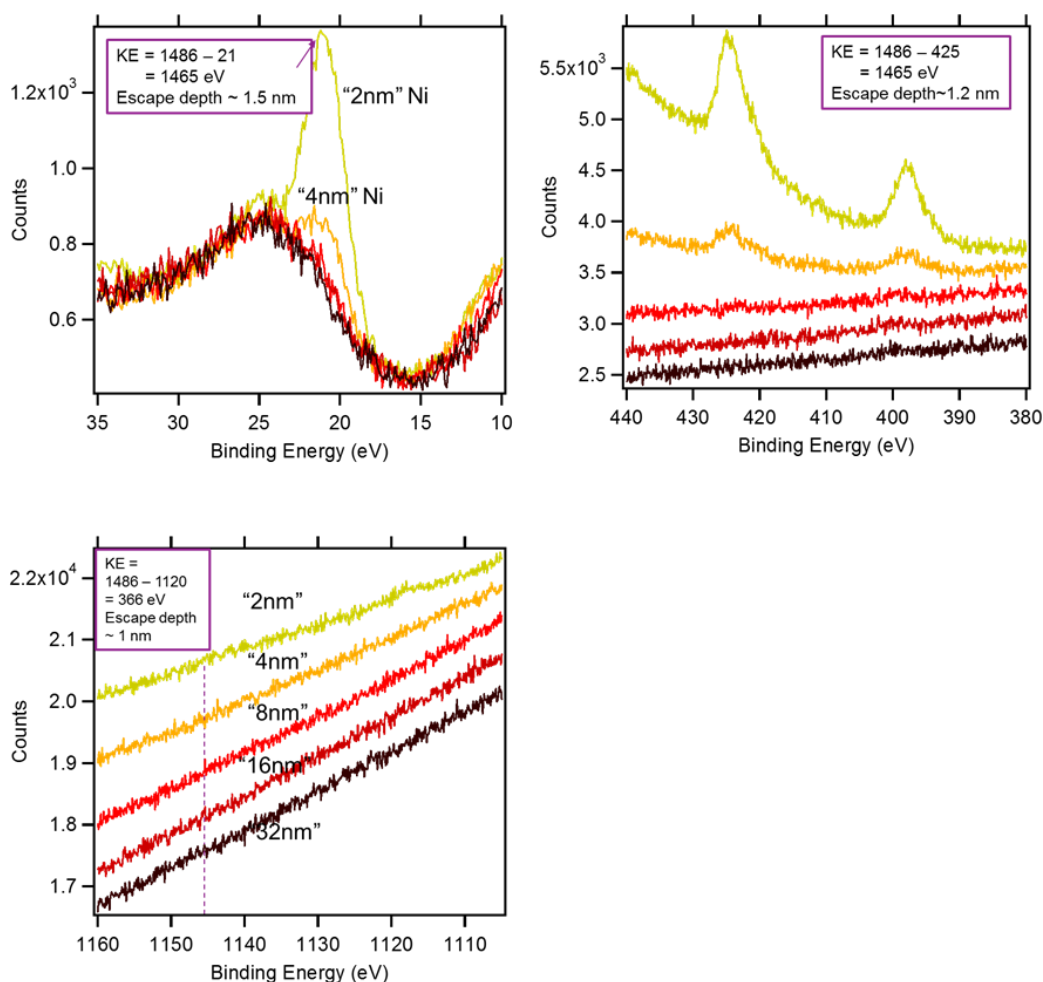

Figure 3.19. Ga XPS for different Ni thickness on top.

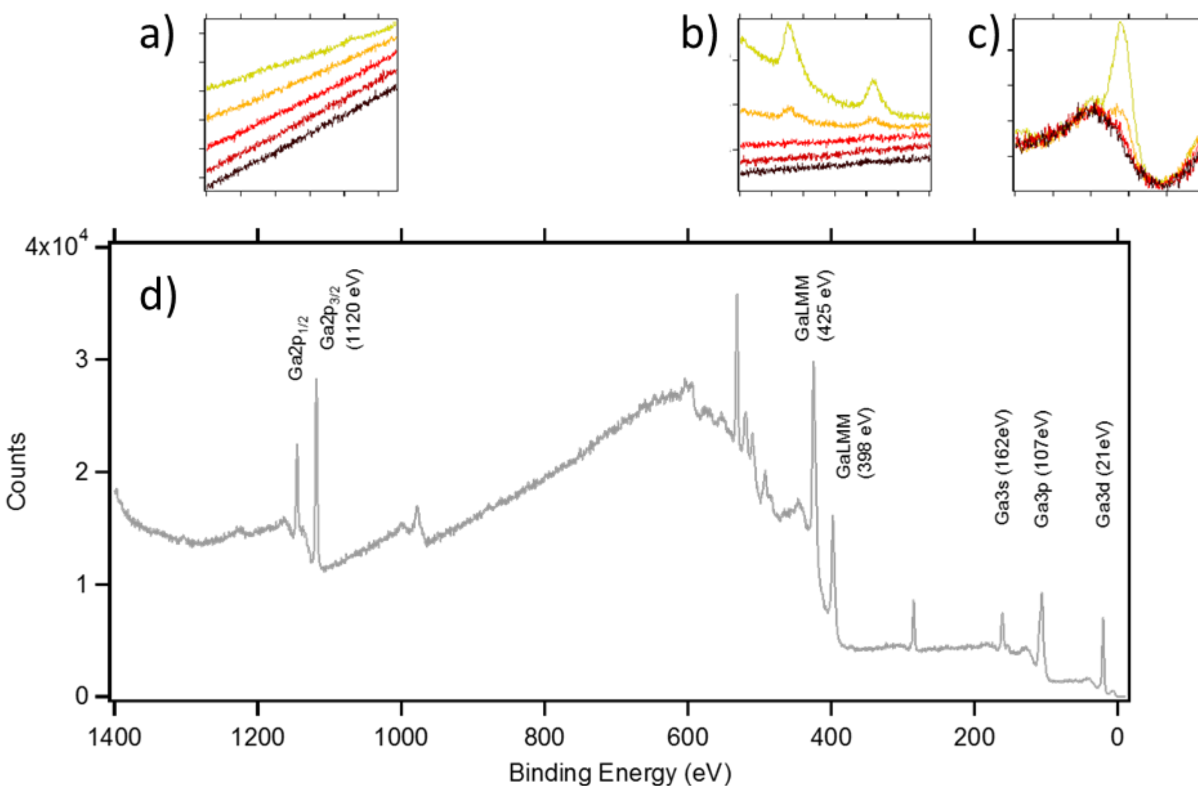

Figure 3.20. XPS high resolution scan of Ga2p (a), GaLMM (b), Ga3d (c) for various thickness of top Ni contact on Ga_2O_3, and survey scan of pure Ga_2O_3 (d).

3.4.4 *Probing of Ni/Ga_2O_3 Interface via XPS through Electron Transparent Layer*

3.4.4.1 Comparison of XPS between ON/OFF states

We have compared the XPS spectra of a Ga_2O_3 switching device with 2nm Ni contact on top. One particular issue with a contact so thin is that handling must be very careful while performing I-V measurement at probe station. In the last section we have shown that the 2nm Ni contact was covering the whole device cell area without significant agglomeration exposing the underneath Ga_2O_3 layer. While applying voltage through a probe, a flattened Indium ball was attached to the tip making a dull contact to thin Ni surface so as to reduce the risk as much as possible of poking through Ni contact. Survey scans show no sign of In after I-V measurement.

As seen in Figure 3.21, we can see a clear difference before and after the electrical treatment. In particular, all Ga peaks have shown significant increase in intensity after switched ON, with Ga2p peaks being the most prominent. Qualitatively, this indicates that Ga migrates towards the surface under electrical treatment. This result is in good agreement with the conclusion from sputtering profile technique, proving that both techniques are useful in studying interface.

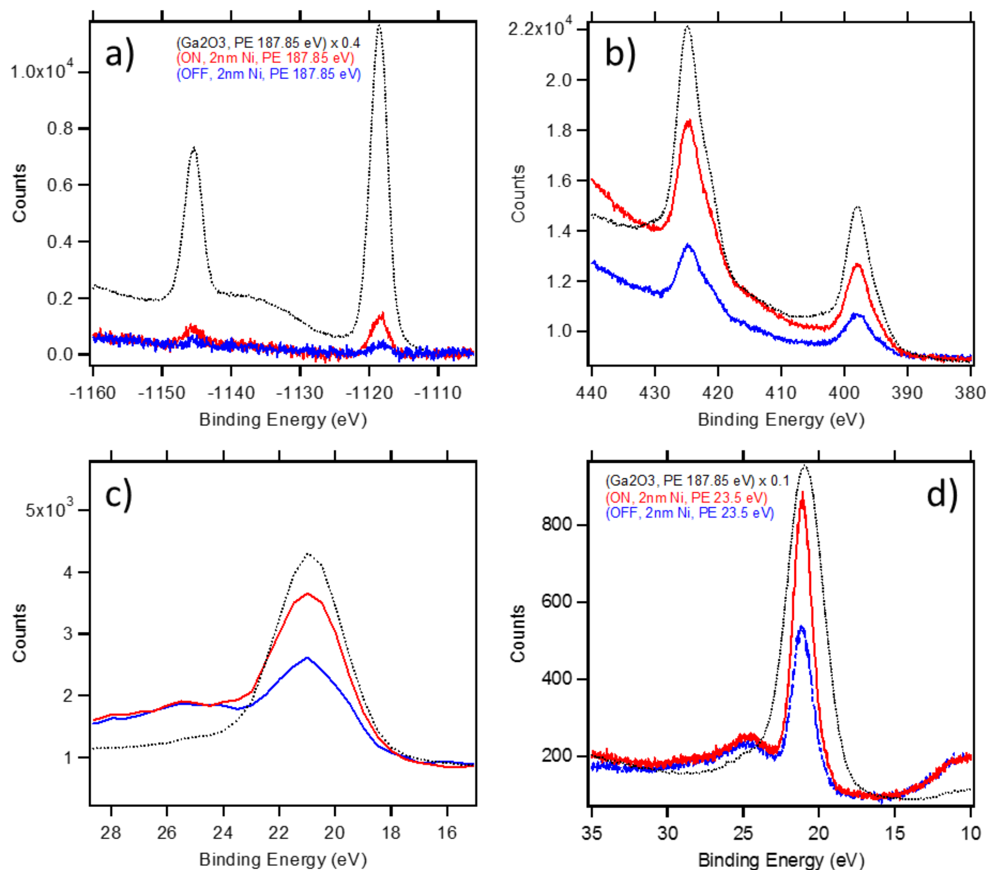

Figure 3.21. Ga peaks of ON(red), OFF(blue) states of 2nm Ni/Ga_2O_3, and pure Ga_2O_3 (black, signal x0.4 except for bottom right which is x 0.1).

So how does these intensity change relates to the Ga migration quantitatively? As shown in the table 3.1, we can calculate the peak intensity ratio of ON/surface Ga_2O_3, and OFF/surface Ga_2O_3. If Ga XPS signal were truly attenuated by an over layer of Ni, the relative peak intensity of all three peaks should essentially correspond to the value at the red and blue line in Figure 3.21.

Table 3.1 Calculation of Ga Migration

	Ga3d (Sv)	Ga3d (Sv)%	d_Ni (nm) from NIST	GaLMM	GaLMM%	d_Ni (nm) from NIST	Ga2p	Ga2p%	d_Ni (nm) from NIST	Avg d (nm)
Ga2O3	26919	100%		144250	100%		95548	100%		
ON	8640.3	32.1%	1.3	31707	22.0%	1.35	4245	4.4%	1.2	1.28
OFF	5356.7	19.9%	1.9	12983	9.0%	2.1	866.32	0.9%	1.8	1.93
OFF/ON		62.0%			40.9%			20.4%		d_OFF-d_ON: 0.65

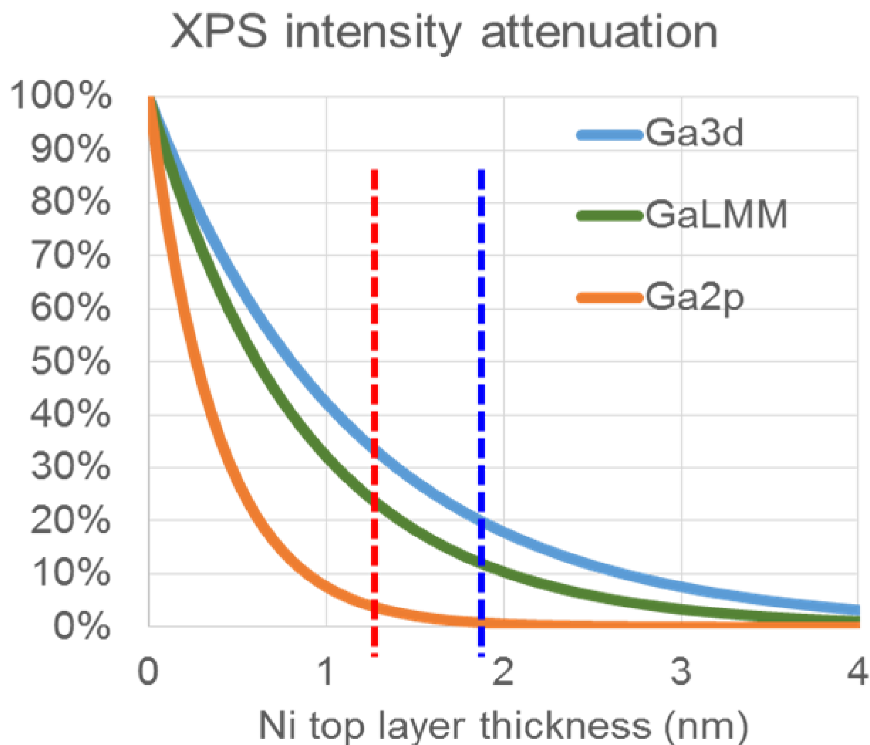

Figure 3.22. ON vs OFF Ga migration.

Indeed, the peak ratio of ON/surface Ga_2O_3 for all three peaks, Ga2p, Ga3d, and GaLMM, correspond very well to an effective attenuation by a Ni over layer of ~ 1.93 nm. Whereas the peak ratio of OFF/surface Ga_2O_3 correspond to an attuation by ~1.28 nm thick of Ni layer. Were these Ga to be emmerging all the way to the surface upon switching, we would have expected roughly the same ratio increase for all three peaks, i.e.

[Ga2p (ON)-Ga2p(OFF)]/Ga2p (surface Ga_2O_3) =

[GaLMM (ON)-GaLMM(OFF)]/GaLMM (surface Ga_2O_3) =

[Ga3d (ON)-Ga3dOFF)]/Ga2p (surface Ga_2O_3)

The fact that this is not the case indicates that Ga were indeed still burried underneath Ni, instead of migrating all the way to the interface. Specifically, Ga seems to migrated ~0.65nm towards the surface, which correspond to about one monolayer or two Ga_2O_3, which is comparrable to the thickness of an interface layer, considering the film could be rather rough for as grown amorphous Ga_2O_3 and subsequent Ni sputtering growth. This gives us significant support of idea that these Ga that migrates toward the interface could be responsible for the switching bahavior.

Detailed fitting are shown below. Notice that for GaLMM, it does not have a specific line shape as core level voigt shape. However, the purse in this practise to get the area under peak. Therefore enough multiple voigt peaks are used until the overall lineshape matches the raw data. For GaLMM, it could also be tricky for the background since it rides on a big shower of inelastically scattered electrons. Linear background shape are used and Shirley integration are not considered in this case for simplicity. For these reasons, one may expect to trust the accuracy of the peak fitting of Ga3d more than GaLMM.

Further more the noise to signal ratio of Ga 2p is rather high due to low intesnisty of Ga peak. Shown are peaks after background subtraction. Statistics of Ga 2p for OFF state is especially poor. Therefore discretion is needed when using these data for physical explanation.

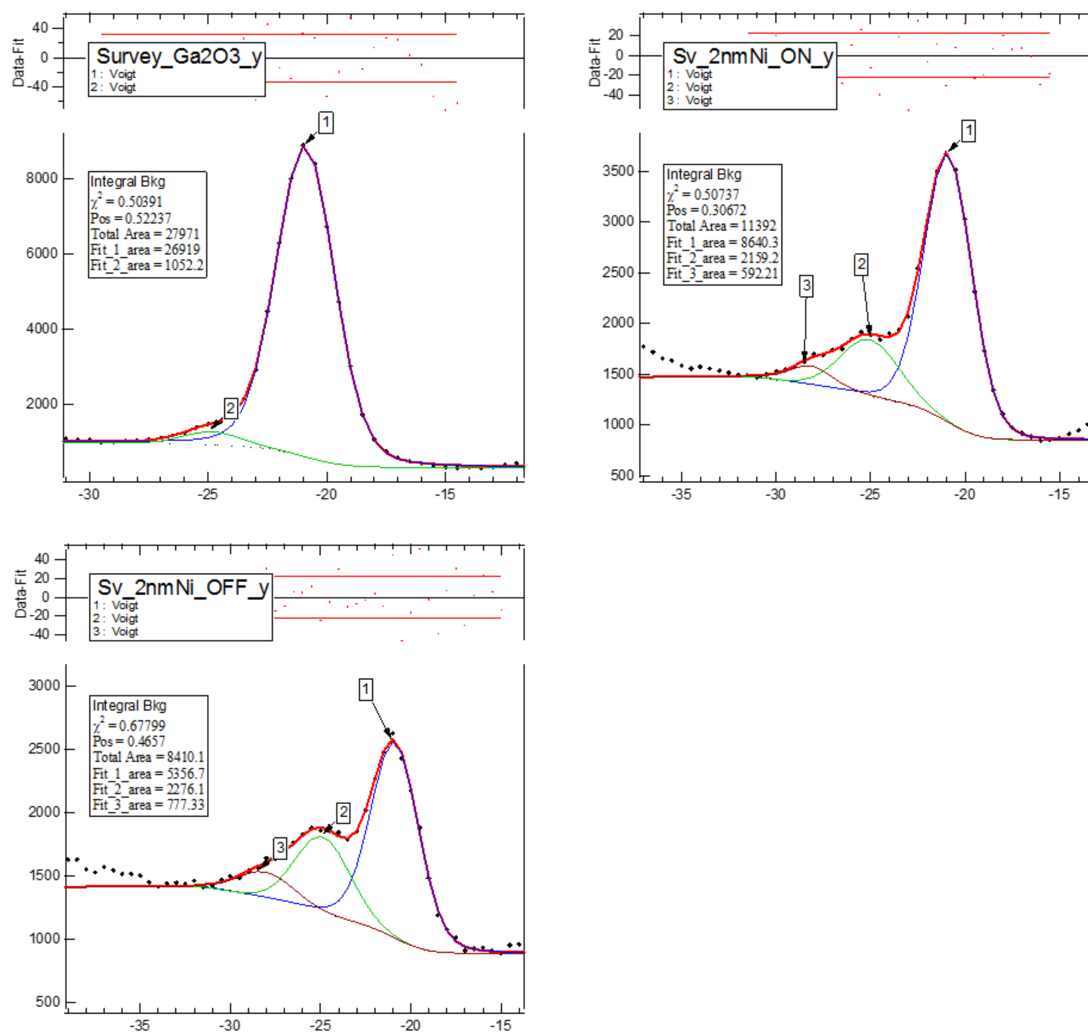

Figure 3.23. peak area fitting of Ga3d.

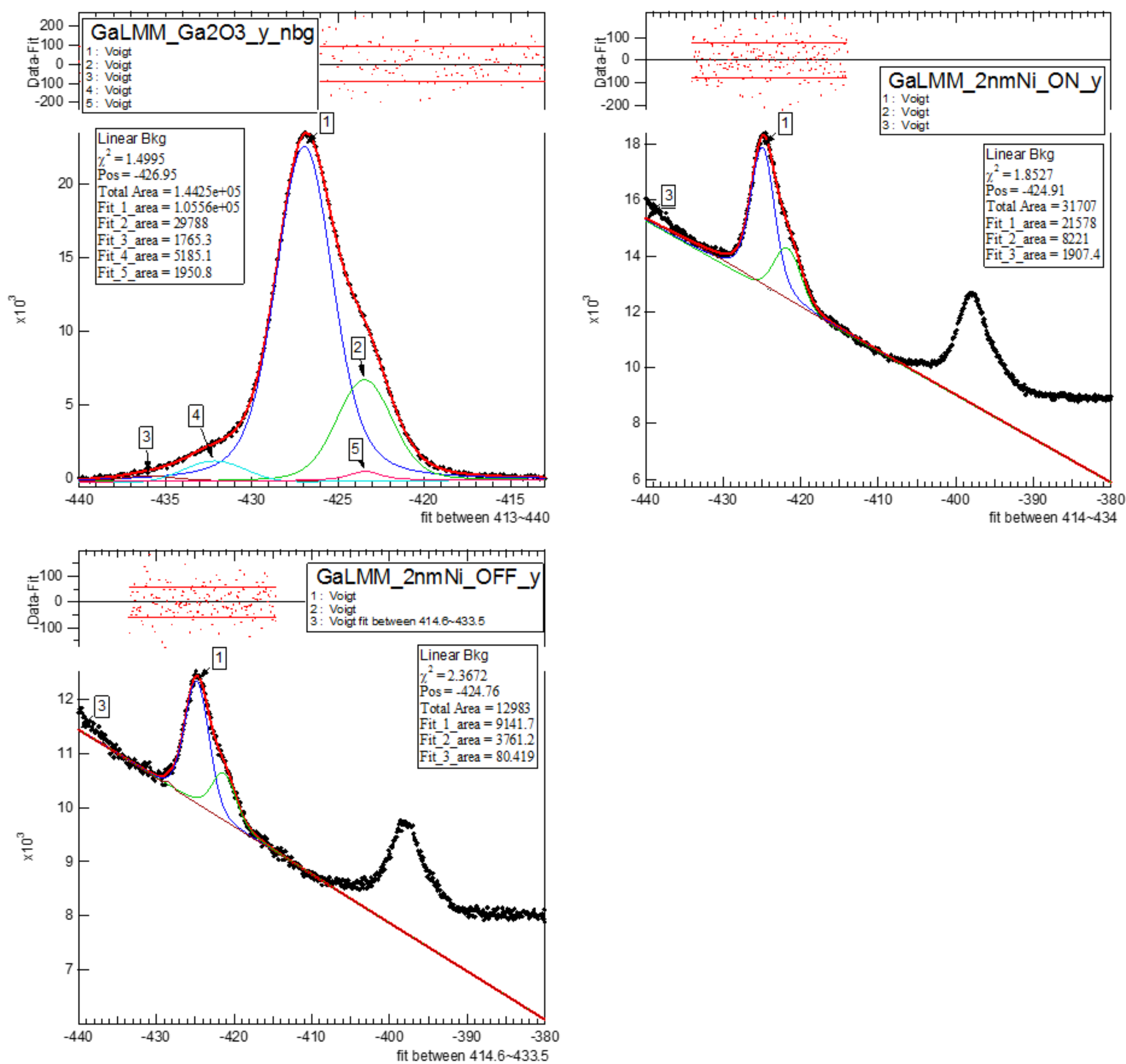

Figure 3.24. peak area fitting of GaLMM.

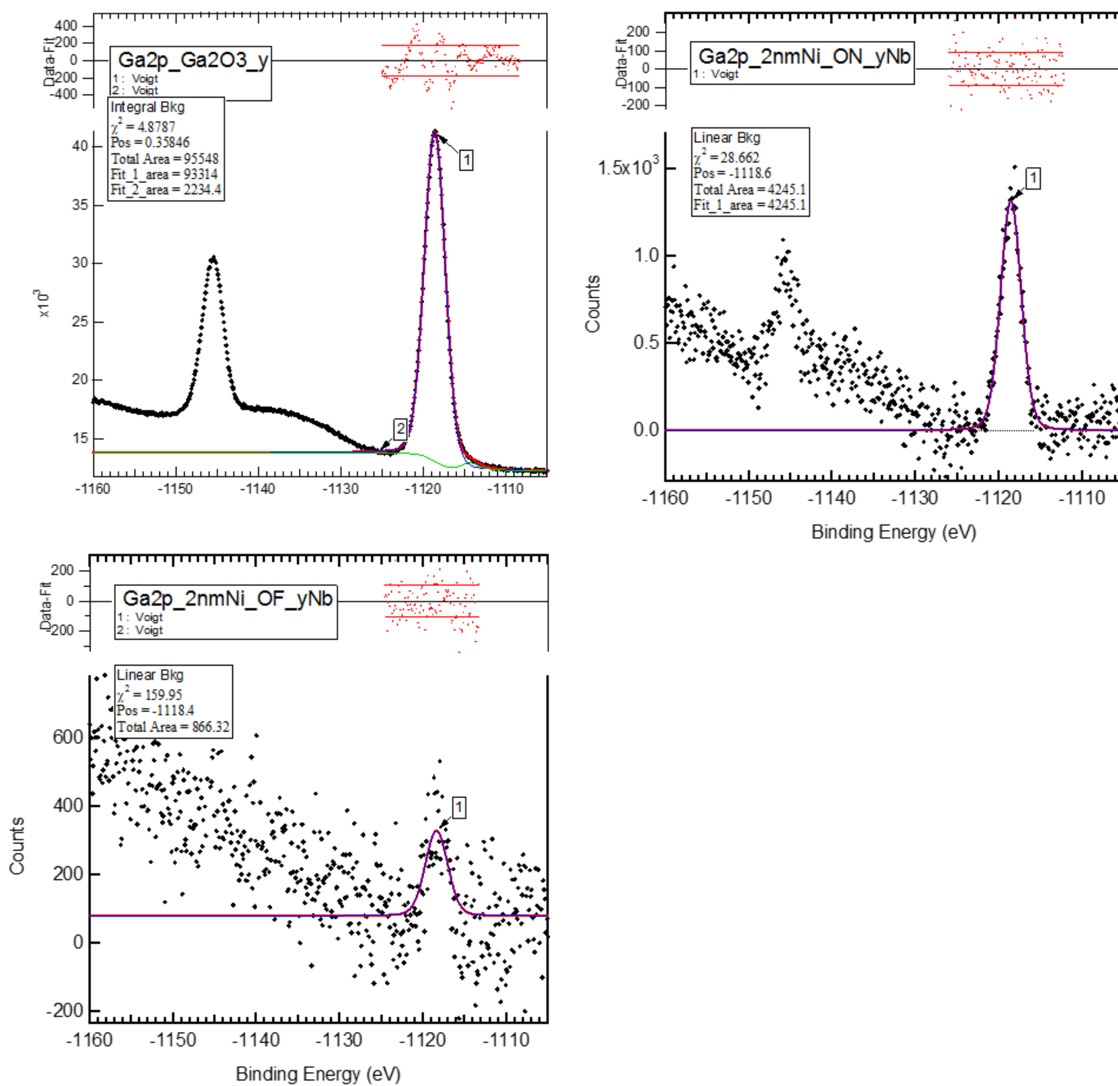

Figure 3.25. peak area fitting of Ga2p.

3.4.5 *Proposed switching mechanism*

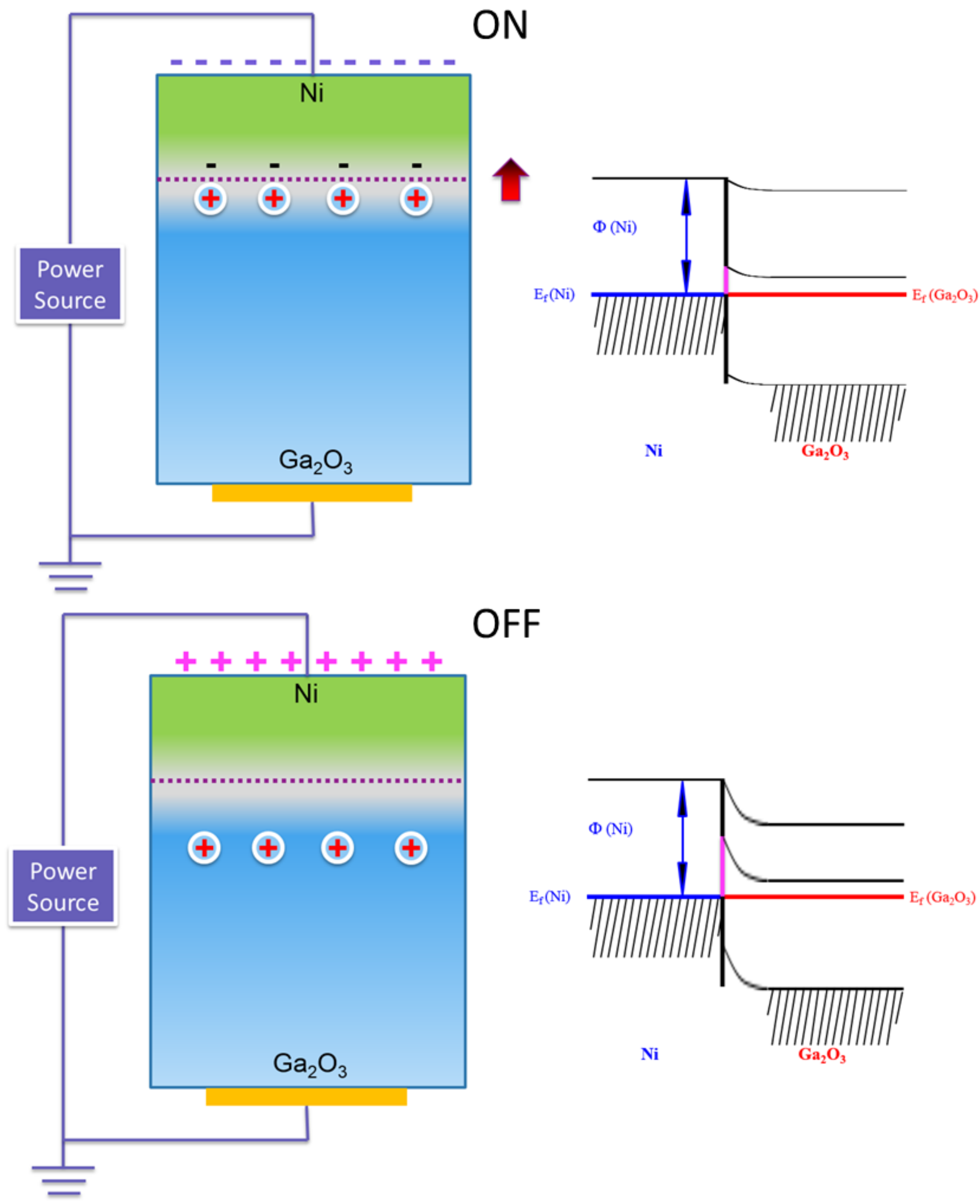

Figure 3.26. resistive switching mechanism by ion migration.

From the analysis above, both sputtering profile and electron transparent top contact XPS results indicate a migration of Ga towards the surface direction as the device is switched ON. A feasible possibility of switching mechanism associated with the phenomenon therefore can be derived as follow. As the top Ni contact is put in negative bias, field driven migration of Ga3+ is undertaken by being attracted to the negative voltage at the surface of Ni. Resulted migrated Ga3+ are therefore accumulated at the interface. Such accumulation of positive charges could induce negative image charge at the Ni side near the interface, form a dipole layer. An illustration is shown in the Figure 3.26 above, this dipole layer that is positive on the semiconductor side will effectively increase the work function of the semiconductor (i.e. more difficult for electron to escape the semiconductor). If such dipole moment are significant enough to lower the work function on the semiconductor side to be closer to the work function of the metal (to about 1 eV as indicated in the table below[82]), then the Schottky barrier can be significantly lowered, or even completely disappear, transforming from Schottky to Ohmic contact, and hence changes the total resistance of the device from high resistive state to low resistive state.

Table 3.2 work function of Ni and Ga_2O_3[82]

	Ni
ΔH_f, kJ/mol of O	-240
Metal work function Φ_m (eV)	5.15
$\Phi_m - \Phi_{Ga2O3}$ (eV)	1.15
measured Φ_B (eV)	0.9**
Depletion width (nm)	200
Carrier concentration (cm^{-3})	$\sim 2.5 \times 10^{15}$

3.5 SUMMARY AND FUTURE WORK

3.5.1 *Previous work summery*

We have successfully made resistive switching unit with Ni/Ga_2O_3/Ir heterostructure. Such device shows reversible switching between one or two orders of magnitude difference in resistance. Device is non-volatile and have good reproducibility. Proposed mechanism in such switching involves Ga migration in and out of the interface driven by electrical field switching the barrier type between Schottky and Ohmic. To test this hypothesis, XPS is utilized to detect interface behavior. Two methods were used to compensate each other. One is removing Ni contact via sputter profile. Optimization of experimental parameters were done using well calibrated Ni/Ti multilayer films. Preliminary results of sputtering profile showing Ga migration towards the interface after switching. The other method used is probing interface through electron transparent thin top contact via XPS. Such non-destructive method showed a significant intensity change in Ga peaks after electrical treatment.

3.5.2 *Continuing sputtering profile on M/Ga_2O_3/M*

For furutre work, with the comprehensive knowledge of XPS sputtering profile technique gained from Ni/Ti multilayer system, we will be able to reliably investigate on Ni/Ga_2O_3 interface, especially comparing any changes between as-grown, HRS, and LRS samples in their element migration, element chemical states, and any other information we could learn to reveal the mechanism of Ga_2O_3 resistive switching behavior.

Reproducibility of switching related spectra change by XPS – in-situ sample prep chamber: It is suspected that structural and chemical change between ON and OFF state of a switching cell could be fairly subtle. Therefore, any conclusion drawn from XPS requires confirmation of reproducible change. Thin contact method is especially useful since it is a non-destructive method and changes can be drawn from the same device as it was switched ON and OFF repeatedly. What's more, as shown in Figure 3.26, signal of oxygen from surface C-O and O-H groups can significantly mask what's accountable for the O inside Ga_2O_3.

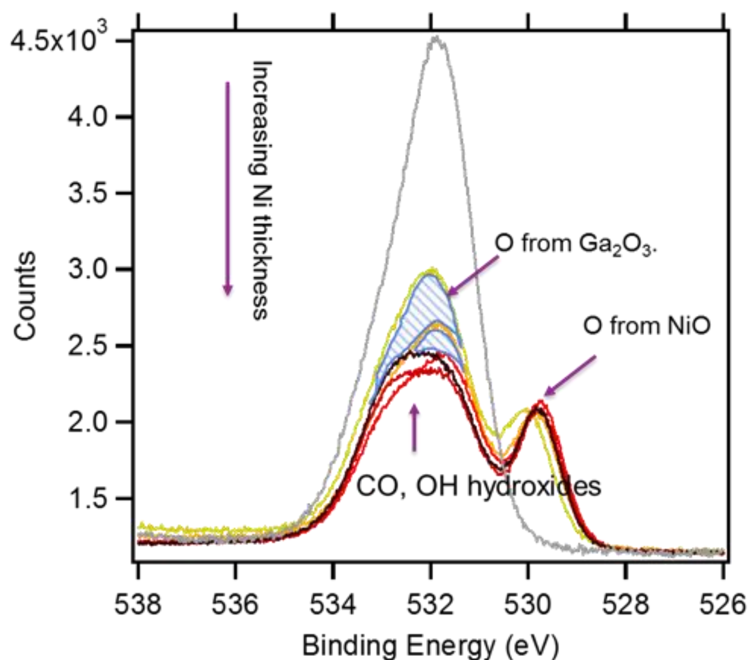

Figure 3.27. O1s for Ga_2O_3 with different Ni thickness top layers.

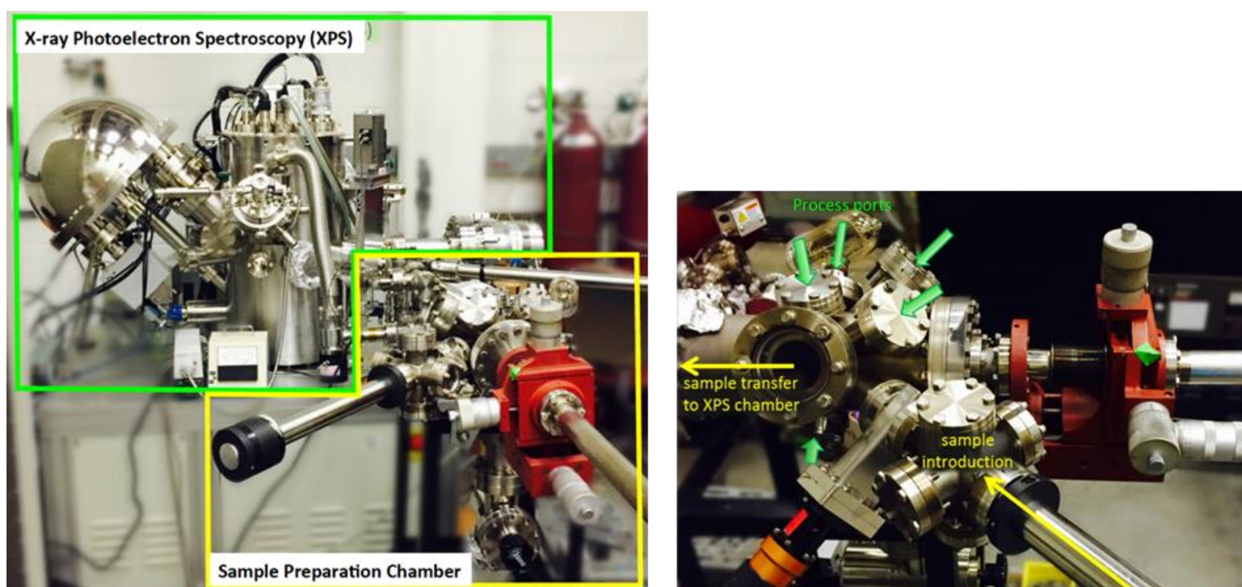

Figure 3.28. XPS Sample Preparation Chamber.

For this purpose, we are currently developing an in-situ multi-functional sample preparation chamber that can be attached to XPS. In detail, a sample is introduced and processed in a preparation chamber, where multiple processing capabilities are available including heating, UV/VIS irradiation, patterned thin film deposition, inert/reactive gas/plasma exposure, electrical

treatment/measurement etc., followed by examining the surface in an analysis chamber using surface sensitive spectroscopy techniques, such as X-ray photoelectron spectroscopy (XPS) and/or ultraviolet photoelectron spectroscopy (UPS); the changes induced by the processing can be determined "in-situ". We are currently building the is-SPC facility in PAB049, and photographs shown in Figure 3.27 depict current status of the system construction. Such facility can allow us to switch the device back and forth and follow up with XPS to see any changes without taking the sample out of vacuum chamber. It would provide more definitive information on switching related structural changes. We believe that combining XPS sputtering profile, alternate depth-profile, and in-situ electrical treatment technique would enable us reveal the true nature of the interface behavior unambiguously, shed lights on the switching mechanism, and provide a platform for any other interface studies in the future that intrigues us.

BIBLIOGRAPHY

1 S. A. Chambers, Weinheim, 2010), Vol. 22, p. 219.

2 B. Zhao, T. Kaspar, T. Droubay, J. McCloy, M. Bowden, V. Shutthanandan, S. Heald, and S. Chambers,"Electrical transport properties of Ti-doped Fe2O3 (0001) epitaxial films", Physical Review B **84**, 245325 (2011).

3 G. E. Brown, V. E. Henrich, W. H. Casey, D. L. Clark, C. Eggleston, A. Felmy, D. W. Goodman, M. Grätzel, G. Maciel, M. I. McCarthy, K. H. Nealson, D. a. Sverjensky, M. F. Toney, and J. M. Zachara,"Metal Oxide Surfaces and Their Interactions with Aqueous Solutions and Microbial Organisms", Chemical Reviews **99**, 77 (1999).

4 Y.-S. Hu, A. Kleiman-Shwarsctein, A. J. Forman, D. Hazen, J.-N. Park, and E. W. McFarland,"Pt-doped alpha-Fe2O3 thin films active for photoelectrochemical water splitting", Chemistry of Materials **20**, 3803 (2008).

5 S. K. Mohapatra, S. E. John, S. Banerjee, and M. Misra,"Water Photooxidation by Smooth and Ultrathin alpha-Fe(2)O(3) Nanotube Arrays", Chemistry of Materials **21**, 3048 (2009).

6 A. Patzelt, H. M. Li, J. D. Wang, and E. Appel,"Palaeomagnetism of Cretaceous to Tertiary sediments from southern Tibet: Evidence for the extent of the northern margin of India prior to the collision with Eurasia", Tectonophysics **259**, 259 (1996).

7 P. W. Schmidt, G. E. Williams, and B. J. J. Embleton,"LOW PALEOLATITUDE OF LATE PROTEROZOIC GLACIATION - EARLY TIMING OF REMANENCE IN HEMATITE OF THE ELATINA FORMATION, SOUTH-AUSTRALIA", Earth and Planetary Science Letters **105**, 355 (1991).

8 T. Droubay, K. M. Rosso, S. M. Heald, D. E. McCready, C. M. Wang, and S. A. Chambers,"Structure, magnetism, and conductivity in epitaxial Ti -doped alpha - Fe2 O3

hematite: Experiment and density functional theory calculations", Physical Review B **75**, 104412 (2007).

9 B. Gilbert, C. Frandsen, E. R. Maxey, and D. M. Sherman,"Band-gap measurements of bulk and nanoscale hematite by soft x-ray spectroscopy", Physical Review B **79**, 035108 (2009).

10 F. J. Morin,"Electrical Properties of α-Fe2O3", Physical Review **93**, 1195 (1954).

11 H. J. Van Daal and A. J. Bosman,"HALL EFFECT IN COO NIO AND ALPHA-FE2O3", Physical Review **158**, 736 (1967).

12 A. J. Bosman and H. J. van Daal,"Small-polaron versus band conduction in some transition-metal oxides", Advances in Physics **19**, 1 (1970).

13 J. B. Goodenough,"Metallic oxides", Progress in Solid State Chemistry **5**, 145 (1971).

14 E. Gharibi, A. Hbika, B. Dupre, and C. Gleitzer,"Electrical-properties of pure and titanium-doped hematite single-crystals, in the basal-plane, at low oxygen-pressure", European Journal of Solid State and Inorganic Chemistry **27**, 647 (1990).

15 K. M. Rosso, D. M. A. Smith, and M. Dupuis,"An ab initio model of electron transport in hematite (α-Fe2O3) basal planes", Journal of Chemical Physics **118**, 6455 (2003).

16 T. Nakau,"Electrical conductivity of alpha-Fe2O3", J. Phys. Soc. Jpn. **15**, 727 (1960).

17 F. J. Morin,"Electrical properties of alpha-Fe2oO3 and alpha-Fe2O3 containing titanium", Physical Review **83**, 1005 (1951).

18 G. A. Acket and J. Volger,"Electric transport in n-type Fe_2O_3", Physica **32**, 1543 (1966).

19 S. A. Chambers, Y. Liang, and Y. Gao,"Noncommutative band offset at α-Cr2O3/α-Fe2O3(0001) heterojunctions", Physical Review B **61**, 13223 (2000).

20 H. Muta, K. Kurosaki, M. Uno, and S. Yamanaka,"Thermoelectric properties of Ti- and Sn-doped α-Fe2O3", Journal of Alloys and Compounds **335**, 200 (2002).

[21] J. A. Glasscock, P. R. F. Barnes, I. C. Plumb, and N. Savvides,"Enhancement of photoelectrochemical hydrogen production from hematite thin films by the introduction of Ti and Si", J. Phys. Chem. C **111**, 16477 (2007).

[22] N. Uekawa, M. Watanabe, K. Kaneko, and F. Mizukami,"Mixed-valence formation in highly oriented Ti-doped iron oxide film", Journal of the Chemical Society, Faraday Transactions **91**, 2161 (1995).

[23] J. S. McCloy, J. V. Ryan, T. Droubay, T. C. Kaspar, S. Chambers, and D. C. Look,"Magnetotransport properties of high quality Co:ZnO and Mn:ZnO single crystal pulsed laser deposition films: pitfalls associated with magnetotransport on high resistivity materials", Review of scientific instruments **81**, 063902 (2010).

[24] J. A. Maxwell, J. L. Campbell, and W. J. Teesdale,"The Guelph PIXE software package", Nuclear Instruments and Methods in Physical Research Section B **43**, 218 (1989).

[25] T. C. Kaspar, T. Droubay, V. Shutthanandan, S. M. Heald, C. M. Wang, D. E. McCready, S. Thevuthasan, J. D. Bryan, D. R. Gamelin, A. J. Kellock, M. F. Toney, X. Hong, C. H. Ahn, and S. A. Chambers,"Ferromagnetism and structure of epitaxial Cr-doped anatase TiO2 thin films", Phys. Rev. B **73** (2006).

[26] E. N. Maslen, V. A. Streltsov, N. R. Streltsova, and N. Ishizawa,"SYNCHROTRON X-RAY STUDY OF THE ELECTRON-DENSITY IN ALPHA-FE2O3", Acta Crystallogr. Sect. B-Struct. Commun. **50**, 435 (1994).

[27] R. D. Shannon,"REVISED EFFECTIVE IONIC-RADII AND SYSTEMATIC STUDIES OF INTERATOMIC DISTANCES IN HALIDES AND CHALCOGENIDES", Acta Crystallographica Section A **32**, 751 (1976).

[28] B. A. Wechsler and C. T. Prewitt,"CRYSTAL-STRUCTURE OF ILMENITE (FETIO3) AT HIGH-TEMPERATURE AND AT HIGH-PRESSURE", Am. Mineral. **69**, 176 (1984).

[29] D. K. Schroder, *Semiconductor Material and Device Characterization* (John Wiley & Sons, New York, 2006).

[30] P. Liao, M. C. Toroker, and E. a. Carter,"Electron transport in pure and doped hematite", Nano Letters **11**, 1775 (2011).

[31] N. Iordanova, M. Dupuis, and K. M. Rosso,"Charge transport in metal oxides: A theoretical study of hematite alpha-Fe2O3", Journal of Chemical Physics **122**, 144305 (2005).

[32] R. F. G. Gardner, F. Sweett, and D. W. Tanner,"Electrical properties of alpha ferric oxide .1. Impure oxide", J. Phys. Chem. Solids **24**, 1175 (1963).

[33] P. L. Liao, M. C. Toroker, and E. A. Carter,"Electron Transport in Pure and Doped Hematite", Nano Letters **11**, 1775 (2011).

[34] S. Kerisit and K. M. Rosso,"Computer simulation of electron transfer at hematite surfaces", Geochimica et Cosmochimica Acta **70**, 1888 (2006).

[35] S. Kerisit and K. M. Rosso,"Kinetic Monte Carlo model of charge transport in hematite (alpha-Fe2O3)", Journal of Chemical Physics **127**, 124706 (2007).

[36] I. G. Austin and N. F. Mott,"Polarons in crystalline and non-crystalline materials", Advances in Physics **18**, 41 (1969).

[37] T. Holstein,"Studies of polaron motion .2. The small polaron", Ann. Phys. **8**, 343 (1959).

[38] D. Emin, C. H. Seager, and R. K. Quinn,"Small-Polaron Hopping Motion in Some Chalcogenide Glasses", Physical Review Letters **28**, 813 (1972).

[39] S. M. Sze and J. C. Irvin,"RESISTIVITY MOBILITY AND IMPURITY LEVELS IN GAAS GE AND SI AT 300 DEGREES K", Solid-State Electron. **11**, 599 (1968).

[40] J. Son, P. Moetakef, B. Jalan, O. Bierwagen, N. J. Wright, R. Engel-Herbert, and S. Stemmer,"Epitaxial SrTiO(3) films with electron mobilities exceeding 30,000 cm(2) V(-1) s(-1)", Nat. Mater. **9**, 482 (2010).

[41] N. F. Mott,"Conduction in non-crystalline materials", Philosophical Magazine **19**, 835 (1969).

[42] V. Ambegaokar, B. I. Halperin, and J. S. Langer,"Hopping conductivity in disordered systems", Physical Review B **4**, 2612 (1971).

[43] A. L. Efros and B. I. Shklovskii,"Coulomb gap and low temperature conductivity of disordered systems", Journal of Physics C: Solid State Physics **8**, L49 (1975).

[44] D. Benjelloun, J. P. Bonnet, J. P. Doumerc, J. C. Launay, M. Onillon, and P. Hagenmuller,"Anisotropy of the electrical-properties of iron-oxide alpha-Fe_2O_3", Mater. Chem. Phys. **10**, 503 (1984).

[45] F. Walz,"The Verwey transition-a topical review", Journal of Physics: Condensed Matter **14**, R285 (2002).

[46] M. W. Khan, S. Husain, M. A. M. Khan, M. Gupta, R. Kumar, and J. P. Srivastava,"Small polaron hopping conduction mechanism in Ni-doped LaFeO3", Philosophical Magazine **90**, 3069 (2010).

[47] A. Banerjee, S. Pal, and B. K. Chaudhuri,"Nature of small-polaron hopping conduction and the effect of Cr doping on the transport properties of rare-earth manganite La0.5Pb0.5Mn1-xCrxO3", Journal of Chemical Physics **115**, 1550 (2001).

[48] D. Morris, Y. Dou, J. Rebane, C. E. J. Mitchell, R. G. Egdell, D. S. L. Law, A. Vittadini, and M. Casarin,"Photoemission and STM study of the electronic structure of Nb-doped TiO(2)", Physical Review B **61**, 13445 (2000).

[49] S. A. Chambers, Y. Gao, Y. J. Kim, M. A. Henderson, S. Thevuthasan, S. Wen, and K. L. Merkle,"Geometric and electronic structure of epitaxial NbxTi1-xO2 on TiO2(110)", Surface Science **365**, 625 (1996).

[50] S. Nasrazadani and A. Raman,"The application of infrared-spectroscopy to the study of rust systems .2. Study of cation deficiency in magnetite (Fe3O4) produced during its transformation to maghemite (gamma-Fe2O3) and hematite (alpha-Fe2O3)", Corrosion Science **34**, 1355 (1993).

[51] A. Janotti and C. G. Van de Walle,"Native point defects in ZnO", Physical Review B **76**, 165202 (2007).

[52] A. F. Kohan, G. Ceder, D. Morgan, and C. G. Van de Walle,"First-principles study of native point defects in ZnO", Physical Review B **61**, 15019 (2000).

[53] G. Dearnaley, A. Stoneham, and D. Morgan,"Electrical phenomena in amorphous oxide films", Reports on Progress in Physics **33**, 1129 (1970).

[54] D. Oxley,"Electroforming, switching and memory effects in oxide thin films", Active and Passive Electronic Components **3**, 217 (1977).

[55] H. Pagnia and N. Sotnik,"Bistable switching in electroformed metal–insulator–metal devices", physica status solidi (a) **108**, 11 (1988).

[56] R. Waser, *Nanoelectronics and information technology* (John Wiley & Sons, 2012).

[57] W. Wu, G.-Y. Jung, D. Olynick, J. Straznicky, Z. Li, X. Li, D. Ohlberg, Y. Chen, S.-Y. Wang, and J. Liddle,"One-kilobit cross-bar molecular memory circuits at 30-nm half-pitch fabricated by nanoimprint lithography", Applied Physics A: Materials Science & Processing **80**, 1173 (2005).

[58] J. E. Green, J. W. Choi, A. Boukai, Y. Bunimovich, E. Johnston-Halperin, E. DeIonno, Y. Luo, B. A. Sheriff, K. Xu, and Y. S. Shin,"A 160-kilobit molecular electronic memory patterned at 1011 bits per square centimetre", Nature **445**, 414 (2007).

[59] S. Kaeriyama, T. Sakamoto, H. Sunamura, M. Mizuno, H. Kawaura, T. Hasegawa, K. Terabe, T. Nakayama, and M. Aono,"A nonvolatile programmable solid-electrolyte nanometer switch", IEEE Journal of Solid-State Circuits **40**, 168 (2005).

[60] T. Hickmott,"Low-frequency negative resistance in thin anodic oxide films", Journal of Applied Physics **33**, 2669 (1962).

[61] L. Chua,"Memristor-the missing circuit element", IEEE Transactions on circuit theory **18**, 507 (1971).

[62] R. S. Williams,"How we found the missing memristor", IEEE spectrum **45** (2008).

[63] D. B. Strukov, G. S. Snider, D. R. Stewart, and R. S. Williams,"The missing memristor found", nature **453**, 80 (2008).

[64] O. Kavehei, Y.-S. Kim, A. Iqbal, K. Eshraghian, S. F. Al-Sarawi, and D. Abbott, in *Communications, Circuits and Systems, 2009. ICCCAS 2009. International Conference on* (IEEE, 2009), p. 921.

[65] A. Asamitsu, Y. Tomioka, H. Kuwahara, and Y. Tokura,"Current switching of resistive states in magnetoresistive manganites", Nature **388**, 50 (1997).

[66] M. Kozicki, M. Yun, L. Hilt, and A. Singh,"Applications of programmable resistance changes in metal-doped chalcogenides", Pennington NJ USA: Electrochem. Soc, 298 (1999).

[67] A. Beck, J. Bednorz, C. Gerber, C. Rossel, and D. Widmer,"Reproducible switching effect in thin oxide films for memory applications", Applied Physics Letters **77**, 139 (2000).

[68] R. Waser and M. Aono,"Nanoionics-based resistive switching memories", Nat. Mater. **6**, 833 (2007).

[69] I. Baek, M. Lee, S. Seo, M. Lee, D. Seo, D.-S. Suh, J. Park, S. Park, H. Kim, and I. Yoo, in *Electron Devices Meeting, 2004. IEDM Technical Digest. IEEE International* (IEEE, 2004), p. 587.

[70] D. S. Jeong, H. Schroeder, and R. Waser,"Coexistence of bipolar and unipolar resistive switching behaviors in a Pt⁄TiO2⁄Pt stack", Electrochemical and solid-state letters **10**, G51 (2007).

[71] D. Kim, S. Seo, S. Ahn, D.-S. Suh, M. Lee, B.-H. Park, I. Yoo, I. Baek, H.-J. Kim, and E. Yim,"Electrical observations of filamentary conductions for the resistive memory switching in NiO films", Applied physics letters **88**, 202102 (2006).

[72] B. Choi, D. Jeong, S. Kim, C. Rohde, S. Choi, J. Oh, H. Kim, C. Hwang, K. Szot, and R. Waser,"Resistive switching mechanism of TiO 2 thin films grown by atomic-layer deposition", Journal of Applied Physics **98**, 033715 (2005).

[73] K. Terabe, T. Hasegawa, T. Nakayama, and M. Aono,"Quantized conductance atomic switch", Nature **433**, 47 (2005).

[74] Y. Hirose and H. Hirose,"Polarity-dependent memory switching and behavior of Ag dendrite in Ag-photodoped amorphous As2S3 films", Journal of Applied Physics **47**, 2767 (1976).

[75] Z. Wang, P. B. Griffin, J. McVittie, S. Wong, P. C. McIntyre, and Y. Nishi,"Resistive Switching Mechanism in $\ hbox {Zn} _ {x}\ hbox {Cd} _ {1-x}\ hbox {S} $ Nonvolatile Memory Devices", IEEE electron device letters **28**, 14 (2007).

[76] I. Tilinin, A. Jablonski, J. Zemek, and S. Hucek,"Escape probability of signal photoelectrons from non-crystalline solids: influence of anisotropy of photoemission", Journal of electron spectroscopy and related phenomena **87**, 127 (1997).

[77] C. Powell and A. Jablonski,"Effects of elastic-electron scattering on measurements of silicon dioxide film thicknesses by X-ray photoelectron spectroscopy", Journal of Electron Spectroscopy and Related Phenomena **114**, 1139 (2001).

[78] C. Powell and A. Jablonski,"Comparisons of calculated and measured effective attenuation lengths for silicon dioxide over a wide electron energy range", Surface science **488**, L547 (2001).

[79] A. Jablonski and C. Powell,"Practical expressions for the mean escape depth, the information depth, and the effective attenuation length in Auger-electron spectroscopy and x-ray photoelectron spectroscopy", Journal of Vacuum Science & Technology A: Vacuum, Surfaces, and Films **27**, 253 (2009).

[80] C. Powell and A. Jablonski,"Electron effective attenuation lengths for applications in Auger electron spectroscopy and x-ray photoelectron spectroscopy", Surface and interface analysis **33**, 211 (2002).

[81] C. Powell and A. Jablonski,"NIST Electron Effective-Attenuation-Length Database, Version 1.3, Standard Reference Data Program Database 82, National Institute of Standards and Technology: Gaithersburg, MD, 2011; h ttp", There is no corresponding record for this reference.

[82] H. T. Pham, UNIVERSITY OF WASHINGTON, 2012.